Atmos. Chem. Phys., 25, 7879–7902, 2025
https://doi.org/10.5194/acp-25-7879-2025

Atmospheric Chemistry and Physics
Open Access
EGU

Research article

Atmospheric processing and aerosol aging responsible for observed increase in absorptivity of long-range-transported smoke over the southeast Atlantic

Abdulamid A. Fakoya[1], Jens Redemann[1], Pablo E. Saide[2,3], Lan Gao[1], Logan T. Mitchell[1], Calvin Howes[3], Amie Dobracki[4,a], Ian Chang[5], Gonzalo A. Ferrada[6,7], Kristina Pistone[8,9], Samuel E. Leblanc[8,9], Michal Segal-Rozenhaimer[8,9], Arthur J. Sedlacek III[4], Thomas Eck[10,11], Brent Holben[11], Pawan Gupta[11], Elena Lind[11], Paquita Zuidema[12], Gregory Carmichael[13,14], and Connor J. Flynn[1]

[1]School of Meteorology, University of Oklahoma, Norman, Oklahoma, USA
[2]Institute of the Environment and Sustainability, University of California, Los Angeles, California, USA
[3]Department of Atmospheric and Oceanic Sciences, University of California, Los Angeles, California, USA
[4]Environmental Science and Technologies, Brookhaven National Laboratory, Upton, New York, USA
[5]Department of Earth, Environmental, and Geographical Sciences, The University of North Carolina at Charlotte, Charlotte, North Carolina, USA
[6]Cooperative Institute for Research in Environmental Sciences, University of Colorado, Boulder, Colorado, USA
[7]Global Systems Laboratory, National Oceanic and Atmospheric Administration, Boulder, Colorado, USA
[8]Bay Area Environmental Research Institute, Moffett Field, California, USA
[9]NASA Ames Research Center, Moffett Field, California, USA
[10]Goddard Earth Sciences Technology and Research (GESTAR) II, University of Maryland Baltimore County, Baltimore, Maryland, USA
[11]NASA Goddard Space Flight Center, Greenbelt, Maryland, USA
[12]Department of Atmospheric Sciences, Rosenstiel School, University of Miami, Miami, Florida, USA
[13]Center for Global and Regional Environmental Research (CGRER), University of Iowa, Iowa City, Iowa, USA
[14]Department of Chemical and Biochemical Engineering, University of Iowa, Iowa City, Iowa, USA
[a]now at: Rainmaker Technology Corporation, El Segundo, California, USA

Correspondence: Abdulamid A. Fakoya (abdulamid.fakoya@ou.edu) and Jens Redemann (jredemann@ou.edu)

Received: 15 October 2024 – Discussion started: 13 January 2025
Revised: 18 April 2025 – Accepted: 28 April 2025 – Published: 25 July 2025

Abstract. Biomass burning aerosol (BBA) from agricultural fires in southern Africa contributes about one-third of the global carbonaceous aerosol load. These particles have strong radiative effects in the southeast Atlantic (SEA), which depend in part on the radiative contrast between the aerosol layer in the free troposphere (FT) and the underlying cloud layer. However, there is large disagreement in model estimates of aerosol-driven climate forcing due to uncertainties in the vertical distribution, optical properties, and life cycle of these particles. This study applies a novel method combining remote sensing observations with regional model outputs to investigate the aging of the BBA and its impact on the optical properties during transatlantic transport from emission

Published by Copernicus Publications on behalf of the European Geosciences Union.

sources in Africa to the SEA. Results show distinct variations in extinction Ångström exponent (EAE) and single-scattering albedo (SSA) as aerosols age. Near the source, fresh aerosols are characterized by low mean SSA (0.84) and high EAE (1.85), indicating smaller, highly absorbing particles. By isolating marine contributions from the total column during BBA transport across the SEA, our analysis reveals an initial decrease in BBA absorptivity, with mean FT SSA of 0.87 after 6–7 d, followed by increased absorptivity with mean FT SSA of 0.84 after 10 d, suggesting enhanced absorption due to chemical aging. These findings indicate that BBA becomes more absorbing during extended transport across the SEA, with implications for reducing model uncertainties. Our remote-sensing-based results agree well with previous in situ studies and offer new insights into aerosol–radiation interactions and the energy balance over the SEA.

1 Introduction

Atmospheric aerosols play a crucial role in Earth's energy balance and climate system. Aerosols perturb the vertical temperature structure, altering the atmospheric stability and overall radiation balance through interactions with sunlight via scattering and absorption, known as aerosol–radiation interactions (ARIs) (Santer et al., 1996; Hansen et al., 1997; Ackerman et al., 2000; Koch and Del Genio, 2010; Boucher, 2015; Samset et al., 2018). Aerosols also serve as cloud condensation nuclei (CCN) or ice-nucleating particles (INPs) that influence cloud microphysics and modify cloud reflectivity (Twomey, 1974, 1977) and lifespan (Albrecht, 1989) through aerosol–cloud interactions (ACIs) (Ackerman et al., 2000; Boucher, 2015). The resulting impacts of ARI and ACI on climate are cumulatively quantified as climate forcing, and its magnitude and sign depend on several factors, including particle size, composition, concentration, mixing state, optical properties, and vertical distribution at a given location.

Single-scattering albedo (SSA), the ratio of aerosol scattering to aerosol extinction and an indicator of aerosol absorptivity, is an important parameter in deriving the radiative effects of aerosols (Chylek and Wong, 1995; Takemura et al., 2002; Bergstrom et al., 2007; Satheesh et al., 2010). Non-absorbing aerosols have SSA of 1, whereas absorbing aerosols have lower values (Moosmüller et al., 2012). The magnitude of the direct aerosol radiative effect depends on the interplay between the radiative properties of aerosols and the underlying scene (Keil and Haywood, 2003; Chand et al., 2009). Non-absorbing aerosols more effectively elevate the scene albedo in regions with inherently darker scenes, whereas absorbing aerosols decrease the albedo most strongly over brighter surfaces, with a comparatively lesser impact over darker surfaces (Mishra et al., 2015; Bellouin et al., 2020). On the global average for radiative forcing, absorbing aerosols exert a cooling effect at the top of the atmosphere. In clear-sky maritime scenarios, this radiative forcing is negative. However, when clouds are present in certain regions such as the southeast Atlantic (SEA), the interaction between aerosol and cloud layers can lead to positive radiative forcing, contingent upon the vertical distribution of the aerosols relative to the clouds (Haywood and Shine, 1997; Keil and Haywood, 2003; Chand et al., 2009).

Biomass burning (BB) is the largest source of carbonaceous aerosols globally (Bowman et al., 2009; Vermote et al., 2009; Bond et al., 2013), emitting significant amounts of brown carbon (BrC), light-absorbing organic aerosols, and up to 40 % black carbon (BC), the strongest light-absorbing aerosol component, into the atmosphere (Bond et al., 2004; Andreae and Gelencsér, 2006; Hopkins et al., 2007; Boucher et al., 2013). The composition of BB aerosol (BBA) is highly variable and often depends on the fuel type and burning conditions, with the less efficient smoldering phase of fires having more organic aerosol (OA) and less BC than the flaming phase (Levin et al., 2010; Liu et al., 2014; Laskin et al., 2015; Collier et al., 2016; Zhou et al., 2017; Jen et al., 2019). BrC exhibits lower mass absorption efficiency compared to BC (Alexander et al., 2008; Jimenez et al., 2009). However, in fires where BrC and BC are co-emitted, the absorption properties of BBA can be influenced by the complex composition, which consists of diverse organic compounds capable of oxidation and photochemistry. These reactions, along with particle morphology and the mixing state of the carbonaceous constituents as well as the condensation of gases and other coating materials upon the BC cores, can modify the absorptive characteristics and atmospheric residence time of the aerosols (Lack and Cappa, 2010; Feng et al., 2013; Saleh et al., 2015; Feng et al., 2021; Dobracki et al., 2023). Given the projected global increase in BB events (Keywood et al., 2013; Jones et al., 2022; Tatro and Zuidema, 2025), an understanding of BBA and their spatial and temporal evolution is becoming essential to improve the estimate of their climate forcing.

Southern Africa contributes approximately 35 % of the global biomass burning emissions (Van Der Werf et al., 2010; Granier et al., 2011; Redemann et al., 2021). Annually, between June and October, these emissions are transported westward over the SEA (Holanda et al., 2020) where they overlie a semi-permanent deck of stratocumulus (Sc) cloud (Fig. 1) and occasionally mix into the marine boundary layer (MBL) (Zhang and Zuidema, 2021). Consequently, the region is characterized by heavy periodic loadings of BBA, which represent the global maximum of aerosol optical depth

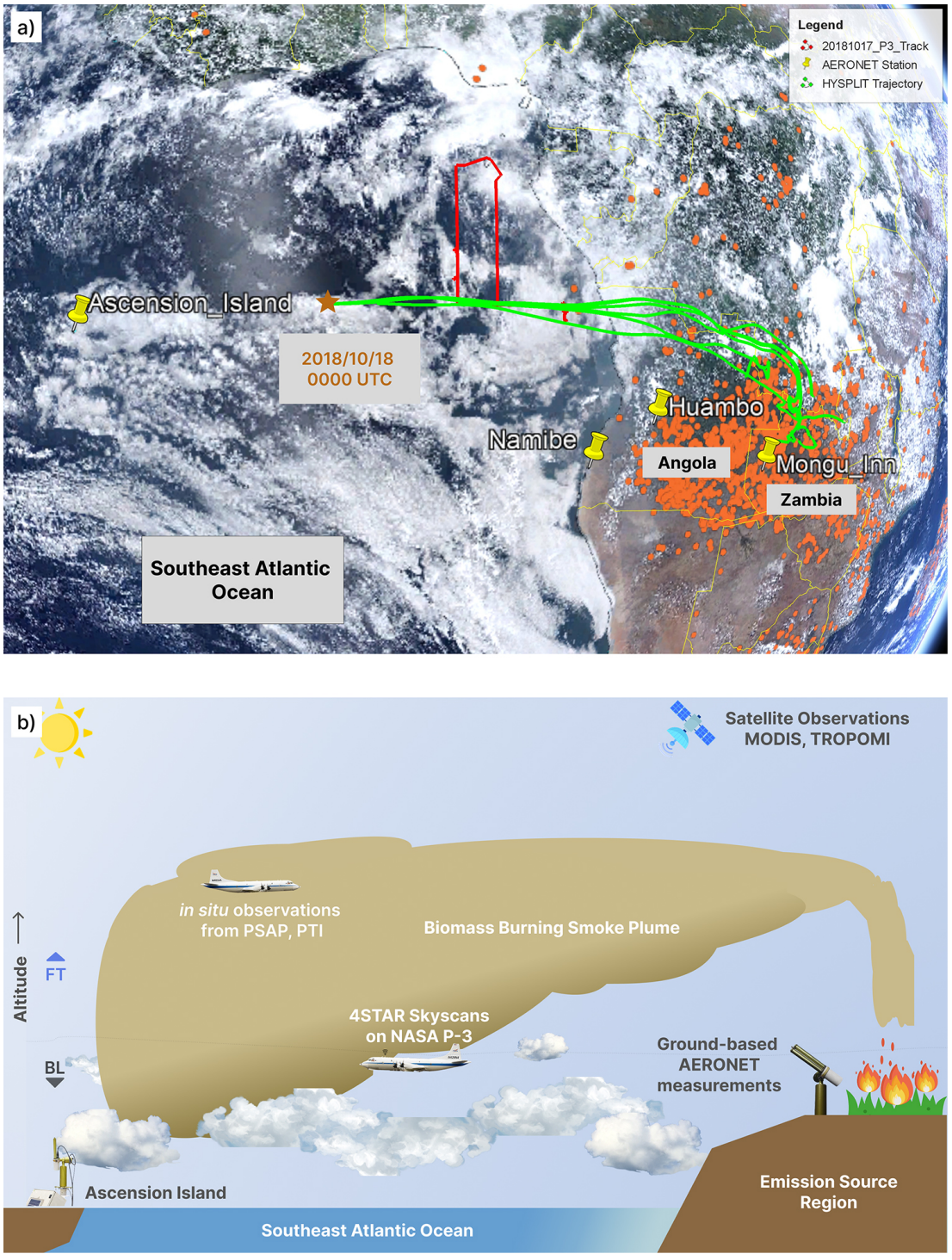

Figure 1. **(a)** Satellite image showing the southeast Atlantic Ocean covered by the stratocumulus cloud deck with smoke being advected over it. The smoke from continental fires (orange dots) is being transported, evident by the 7 d backward HYSPLIT trajectory (green) ending between 4000–5000 m on 18 October 2018, to intersect the P-3 flight (red) on 17 October 2018. Yellow icons represent AERONET stations selected for this study (https://worldview.earthdata.nasa.gov/, last access: 18 April 2025, https://www.ready.noaa.gov/HYSPLIT_traj.php, last access: 18 April 2025, https://earth.google.com, last access: 18 April 2025, https://aeronet.gsfc.nasa.gov/, last access: 18 April 2025). **(b)** Schematic of the collocation of observations in the southeast Atlantic region during the ORACLES mission. Satellite observations are from the Moderate Resolution Imaging Spectroradiometer (MODIS) and TROPOspheric Monitoring Instrument (TROPOMI). Airborne observations are from 4STAR, ground-based observations are from AERONET, and in situ measurements are from the Particle Soot Absorption Photometer (PSAP) and Photo-Thermal Interferometric (PTI) Particle Absorption Monitor. Measurements from 4STAR and AERONET are presented in this study.

(AOD) above clouds (Waquet et al., 2013; Adebiyi et al., 2015).

BBA in this region typically has SSA values ranging between 0.7 and 0.9 from observations (Dubovik et al., 2002; Haywood et al., 2003; Eck et al., 2013). These values generally increase from July to November (Eck et al., 2013), with an average value of 0.85 during the burning season (Leahy et al., 2007; Eck et al., 2013; Pistone et al., 2019; Dobracki et al., 2023), indicating their significant ability to absorb sunlight. BBA also serves as CCN and accounts for approximately 65 % of the total CCN in the Sc cloud deck of the SEA (Andreae and Rosenfeld, 2008; Che et al., 2021; Lenhardt et al., 2023; Dedrick et al., 2024). The warming effect and the ACI by BBA are not well represented in Earth system models (ESMs), and the SEA region exhibits a large model-to-model divergence of climate forcing due to aerosols (Sakaeda et al., 2011; Stier et al., 2013; Che et al., 2021; Mallet et al., 2020; Haywood et al., 2021). Reliable quantification of the climatic effects of BBA requires an accurate representation of aerosol properties and their vertical and horizontal distributions in models.

Despite recent studies that have documented the transport and characterized the chemical, optical, and microphysical properties of the southern African BBA transport (Vakkari et al., 2018; Pistone et al., 2019; Denjean et al., 2020a, b; Holanda et al., 2020; Wu et al., 2020; Baars et al., 2021; Dobracki et al., 2023), it is still not well understood how the properties of these aerosols evolve during long-range transport. The southern African BBA has been associated with the BC-rich pollution layer above the Amazonian basin following extended transport over the SEA (Holanda et al., 2020). Variations in the chemical composition of BBA at different altitude above the Atlantic have been shown to influence the optical properties of aged BBA (Wu et al., 2020), with low SSA values attributed to the presence of strongly absorbing refractory black carbon (rBC) and minimal contribution from BrC (Denjean et al., 2020b). The mixing state of rBC particles (Denjean et al., 2020b; Sedlacek et al., 2022) and the accumulation of a non-absorbing shell by rBC (Redemann et al., 2001) strongly affect the SSA of BBA. Knowledge of the spatial and temporal evolution of BBA, especially during long-range transport, is key to understanding the atmospheric processes affecting their life cycle and their contribution to climate forcing.

While the aging of BBA has recently been parameterized in global climate models (GCMs) (Konovalov et al., 2021; Nascimento et al., 2021), accurately representing the optical and microphysical characteristics of these particles in models remains a challenge due to the intricate chemical and physical processes involved (Brown et al., 2021) and because there have been limited studies on aged BBA. Most research on the evolution and aging of BBA has focused on BBA that has been sampled near the source or in short-term laboratory experiments (Reid et al., 1998; Bond et al., 2006; Kleinman et al., 2020; Feng et al., 2021; Liu et al., 2021; Sedlacek et al., 2022). Due to the lack of observations on longer timescales, a gap exists in our understanding of how the optical properties of BBA change during extended transport, such as that over the SEA. Investigating the evolution of aged BBA is, therefore, crucial for improving model capabilities for representing their optical and radiative properties.

The overarching goal of this study is to examine the evolution of BBA emitted during the annual burning season in southern Africa using remote sensing observations during their transport across the SEA. Studies on BBA in the region have focused primarily on either continental southern Africa (Abel et al., 2003; Eck et al., 2003, 2013; Queface et al., 2011) or over the ocean (Meyer et al., 2013; de Graaf et al., 2014; Zuidema et al., 2018; Pistone et al., 2019; Redemann et al., 2021). Measurements over the ocean from the ORACLES (ObseRvations of Aerosols above CLouds and their intEractionS) campaign dataset highlighted the connection between BBA composition and absorption, showing a decrease in SSA concurrent with the loss of OA coating on rBC particles, as shown by Sedlacek et al. (2022) and Dobracki et al. (2023). However, our study seeks to expand upon these findings by analyzing aerosol absorption along the entire transport pathway of BBA from the emission source to the SEA region (Fig. 1). Here, we develop a new methodology that integrates remotely sensed observations from AERONET (AErosol RObotic NETwork) in the BB emission region and 4STAR (Spectrometers for Sky-Scanning, Sun-Tracking Atmospheric Research) over the ocean, collected during the ORACLES campaign. These observations are combined with aerosol age estimates outputs from the WRF-AAM (Weather Research and Forecasting coupled with Aerosol Aware Microphysics module) regional model (Saide et al., 2016) and aerosol properties derived from WRF-CAM5 (Weather Research and Forecasting coupled with the Community Atmosphere Model version 5). WRF-CAM5 has previously been used to document the chemical composition, hygroscopicity, and aerosol–cloud interactions of BBA in the ORACLES campaign region (Howes et al., 2023). This approach enables a comprehensive assessment of the aging of the smoke plume and its impact on optical properties. Particularly, we use the observation of BBA from ORACLES campaign during the burning season of September 2016, August 2017, and October 2018 to investigate the changes in SSA of BBA during their transatlantic transport, spanning the phases of transport over land and, subsequently, over the SEA. Furthermore, using remote sensing to retrieve SSA offers the advantage of sampling aerosols in their ambient state and can be replicated in other domains where AERONET observations are available.

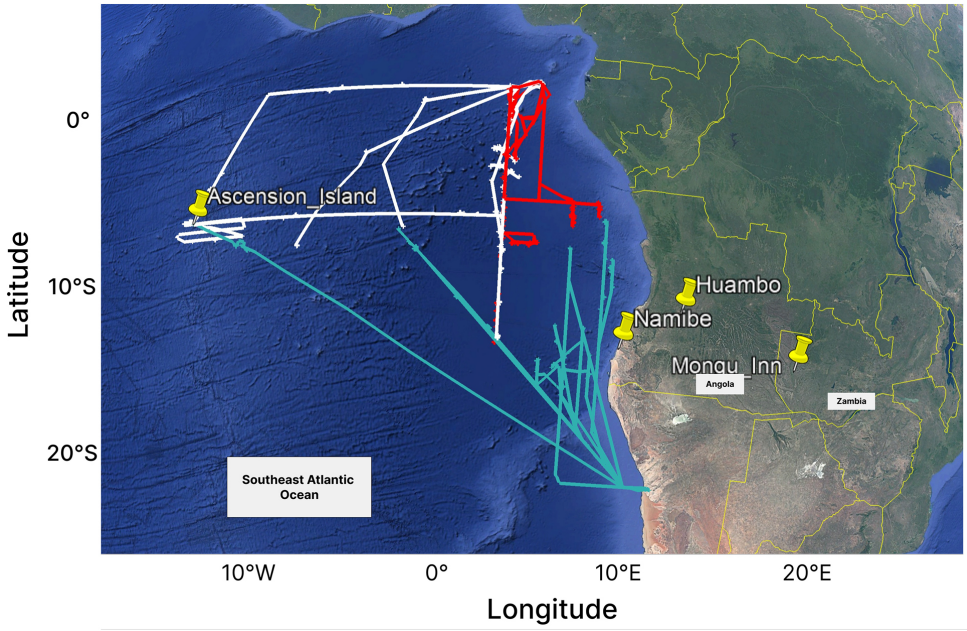

Figure 2. Map of the SEA showing the NASA P-3B flight tracks during ORACLES 2016 (cyan), 2017 (white), and 2018 (red) for observation days analyzed in this study. The ORACLES aircraft deployed from Walvis Bay, Namibia, in 2016 and São Tomé and Príncipe in 2017 and 2018. Regional AERONET stations are identified using yellow icons. Background imagery is from © Google Earth (https://earth.google.com, last access: 18 April 2025) – data are from SIO, NOAA, US Navy, NGA, GEBCO; the image is from Landsat/Copernicus.

Table 1. Summary of observation data products and aerosol properties used in this study. The italicized text represents the retrieval wavelengths of the aerosol properties.

Data	Product	Properties	Data access
AERONET	Inversion (level 1.5, 2.0) product version 3: all observations	Aerosol optical depth (AOD) and single-scattering albedo (SSA) *440, 675, 870 nm* Extinction Ångström exponent (EAE) *440–870 nm*	https://aeronet.gsfc.nasa.gov/ (last access: 1 April 2025)
4STAR	4STAR-aeroinv_P3	Aerosol optical depth (AOD) and single-scattering albedo (SSA) *500, 675, 870, 975 nm* Extinction Ångström exponent (EAE) *500–975 nm*	https://espoarchive.nasa.gov/archive/browse/oracles/P3/4STAR-aeroinv (last access: 1 April 2025)

2 Data and methods

2.1 NASA ORACLES campaign

A comprehensive overview of the ORACLES campaign is presented by Redemann et al. (2021). Here, we summarize the methods and data analysis techniques that are relevant to this study. The campaign provided process-level understanding of aerosol effects in the SEA that can be applied in the parameterization of ACI and ARI in ESMs (Redemann et al., 2021). The campaign overlapped with other field experiments (Zuidema et al., 2016) – CLARIFY-2017: Cloud–Aerosol–Radiation Interactions and Forcing for Year 2017 (Haywood et al., 2021), LASIC: Layered Atlantic Smoke Interactions with Clouds (Zuidema et al., 2018), AEROCLOsA: AErosols, RadiatiOn and CLOuds in southern Africa (Formenti et al., 2019) – in a synergistic effort to determine the influence of southern African BBA on cloud properties and the energy balance in the SEA region. The ORACLES campaign occurred between 2016 and 2018 with field deployments in Walvis Bay, Namibia (September 2016), and in São Tomé and Principe (August 2017 and October 2018). The NASA P3-B aircraft was home to a suite of in situ and remote sensing instruments including the 4STAR (Dunagan et al., 2013), and the ER-2 (a high-altitude aircraft) was home to a suite of additional remote sensing instruments. A to-

tal of 56 research flights – 12 from the ER-2, only in 2016, and 44 from the P-3B across the three deployments, shown in Fig. 2, with over 450 science flight hours – collected data on aerosol optical properties (Pistone et al., 2019; Redemann et al., 2021). This study uses 4STAR retrievals of BBA properties (Table 1) from all three campaign deployments made on the P-3B aircraft to study the evolution of the light absorption properties of BBA.

2.2 Ground-based measurements

AERONET, a global sun photometer network, provides long-term, continuous measurement of AOD and retrievals of aerosol microphysical, optical, and radiative properties for aerosol characterization and validation of satellite retrievals (Holben et al., 1998). In this study, we used AERONET version 3 inversion products (Table 1) from both almucantar (ALM) and hybrid scans including cloud-screened (level 1.5) and quality-assured (level 2.0) data (Giles et al., 2019; Sinyuk et al., 2020) from four AERONET stations: three situated in continental southern Africa (Mongu Inn, Zambia; Huambo, Angola; Namibe, Angola) and one in the maritime SEA (Ascension Island, United Kingdom territory) (Table 2). These stations were carefully selected based on their geographic locations aligning with the trajectory of BBA from continental Africa and over the ocean, as shown in Fig. 1. Specifically, column-integrated measurements of AOD, SSA, and the extinction Ångström exponent (EAE) for September 2016, August 2017, and October 2018 were used, coinciding with the observation periods of ORACLES 2016, 2017, and 2018. The Namibe site was inactive during the ORACLES 2018 campaign, providing data only for 2016 and 2017, while the Huambo site, established in 2017, contributed observations for both 2017 and 2018. At Ascension Island and Namibe, fewer observations were available due to the increased cloud cover along the coast and over the SEA. Therefore, to ensure an adequate sample size at Ascension Island and Namibe, we included level 1.5 data in our analysis when level 2.0 data were unavailable. More information about the AERONET stations utilized in this study is provided in Table 2.

2.3 Airborne measurements

This study uses sky radiance measurements from the airborne 4STAR instrument (Dunagan et al., 2013) aboard NASA P-3B aircraft, enabling AERONET-like observations in remote regions beyond ground-based network coverage. Its frequent co-deployment with in situ instrumentation offers a more comprehensive characterization of aerosol properties. This analysis focuses on observations made in the sky-scanning mode (Pistone et al., 2019), using both ALM and principal plane (PPL) scans. Given that most ORACLES flights occurred near solar noon, limiting the angular range of ALM scans, PPL scans were selectively included if they met specific quality control (QC) criteria. Here, we processed 4STAR sky scans using the QC criteria from Mitchell et al. (2023). These criteria were adapted from Pistone et al. (2019) for four-wavelength 4STAR retrieval of ORACLES 2016–2018 and serve as a proxy for AERONET level 1.5 aerosol inversion standards. The criteria are (1) AOD (400 nm) > 0.2, (2) altitude difference < 50 m, (3) sky error < 10 %, (4) minimum scattering angle $< 6°$, (5) maximum scattering angle $> 50°$, (6) mean scattering angle difference $< 3°$ (between 3.5 and 30°), (7) maximum scattering angle difference $< 10°$ (between 3.5 and 30°), (8) roll standard deviation $< 3°$, (9) passing the retrieval boundary test – ensuring that the retrieval is within the limits of parameter space, and (10) maximum altitude < 3000 m. A summary of the valid quality-controlled 4STAR retrievals of SSA, AOD, and EAE (Mitchell et al., 2023) in the ORACLES dataset (Oracles, 2020) for all three deployments is given in Table 1.

2.4 WRF-CAM5: concept and configuration

WRF-CAM5 is an adaptation of the WRF-Chemistry (WRF-Chem) model (Grell et al., 2005), which integrates the physics and aerosol packages of the global CAM5 (Ma et al., 2014; Zhang et al., 2015a), making it suitable for studying multi-scale atmospheric processes and evaluating aerosol and physics parameterizations in global climate models (Wang et al., 2018). WRF-CAM5 has been widely applied to investigate air quality and climate interactions in Asia and the United States (Zhang et al., 2015b; Campbell et al., 2017; Wang et al., 2018) and has shown good skill in capturing smoke concentration, aerosol properties, and the vertical distribution of BBA in the SEA region (Doherty et al., 2022; Chang et al., 2023). In this study, the model is configured at 36 km horizontal resolution with 74 vertical layers over the spatial domain 41° S–14° N, 34° W–51° E, initialized every 5 d using the National Centers for Environmental Prediction (NCEP) Final Operational Global Analysis (NCEP FNL) and Copernicus Atmosphere Monitoring Service (CAMS) reanalysis datasets as detailed in Shinozuka et al. (2020a) and Doherty et al. (2022), with daily smoke emissions from the Quick-Fire Emissions Dataset version 2 (QFED2) (Darmenov and Da Silva, 2015).

2.5 Plume age derivation

To estimate the age of the aerosols, defined as the time since emission, we utilized a carbon monoxide (CO) tracer coupled with smoke emissions within the WRF-AAM model. The WRF-AAM model, which shares similar configurations with WRF-CAM5, allows for region- and case-specific microphysical parameterization of aerosol–cloud interactions (Thompson and Eidhammer, 2014) and aerosol–radiation interactions (Saide et al., 2016), thus facilitating the characterization of aerosol aging processes.

Table 2. Site information and total observation count for AERONET and 4STAR. The italicized text in the header (2016, 2017, 2018) indicates the year corresponding to the observation counts listed in parentheses.

Site name	Latitude	Longitude	Elevation (m)	Number of observations (*2016, 2017, 2018*)
Ascension Island	−7.97	−14.41	30	77 (*17*, *53*, *7*)
Namibe	−15.15	12.17	11	135 (*71*, *64*, –)
Huambo	−12.86	15.7	1670	342 (–, *250*, *92*)
Mongu Inn	−15.26	23.13	1040	444 (*126*, *167*, *151*)
4STAR	–	–	–	308 (*77*, *139*, *92*)

The regional model was set up with a horizontal resolution of 12 km, encompassing the geographical area 41° S–14° N, 34° W–51° E. This domain size is considered sufficiently extensive to contain nearly all fires across the African continent (Saide et al., 2016; Howes et al., 2023). The fire emission source for the model is based on QFED2, which uses fire radiative power (FRP) as a proxy for estimating fire emissions. QFED2 leverages the cloud correction techniques developed in the Global Fire Assimilation System (GFAS) to refine emission estimates (Darmenov and Da Silva, 2015). The location and FRP of fires are sourced from MODIS Level 2 fire products (MOD14 and MYD14), coupled with MODIS Geolocation products (MOD03 and MYD03). The NCEP Global Forecasting System (GFS) meteorology serves as the primary driver for the WRF-AAM model, which incorporates daily smoke emissions from QFED2 that are subsequently adjusted to correspond to satellite-derived AOD using a near-real-time inversion algorithm, as detailed in Saide et al. (2016).

The model was run in a forecast mode to estimate the time since smoke emission, with a maximum aerosol age of 14 d. The model attaches age tracers to the CO released at BB emission sites. These tracers, which are treated as chemically inert gases, are tagged for each day and tracked for up to 2 weeks, allowing sufficient time for the smoke to travel across the SEA. This model setup operates in a cycle, where each day, the tracers from the previous day are shifted to the next older tracer bin, continuing until they reach the 14 d mark. At this point, they accumulate in the oldest bin. The age of the smoke plume is determined by averaging the concentration of these tracers at any given location. However, this setup has limited accuracy at the upper end of the age estimate; for instance, smoke older than 14 d is still averaged as 14 d old, even if it contains an equally concentrated mixture of tracers that have been out for different lengths of time beyond the 14 d tracking period. In comparison, the HYSPLIT model (Stein et al., 2015), also driven by the NCEP GFS meteorology, typically yields age estimates that are approximately 1 d lower than the WRF-AAM. Given that HYSPLIT employs a simpler scheme at coarser resolutions, it is likely that the age estimates from the WRF-AAM model are more accurate and reliable. The plume ages assigned within a given column exhibited minimal variability (see Sect. S6), which gives confidence to the method.

To determine the effective aerosol age for AERONET and 4STAR observations, which are columnar, the WRF-AAM model's assigned plume age in the vertical layers above these instruments is weighted by their respective extinction coefficients (β_{ext}) per Eq. (1):

$$\text{Aerosol age} = \frac{\int_{s_{\text{elv}}}^{\text{TOA}} \beta_{\text{ext}} \times \text{plume age}\, \mathrm{d}z}{\int_{s_{\text{elv}}}^{\text{TOA}} \beta_{\text{ext}}\, \mathrm{d}z}, \quad (1)$$

where s_{elv} is the elevation of the AERONET station or the flight altitude of observation for 4STAR and TOA is the top of the atmosphere.

2.6 Spatiotemporal collocation and analysis

The AERONET inversion products provide AOD and SSA at four wavelengths: 440, 675, 870, and 1020 nm. The relationship between AOD and wavelength, defined by the Ångström exponent formula (Eck et al., 1999), is used to compute EAE(α):

$$\text{EAE}(\alpha) = -\frac{\ln(\tau_1) - \ln(\tau_2)}{\ln(\lambda_1) - \ln(\lambda_2)}, \quad (2)$$

where τ_1 and τ_2 are AOD at wavelengths λ_1 and λ_2. In AERONET and 4STAR retrievals, EAE(α) is calculated from AOD measurements at 440 and 870 nm.

Given the differences in the temporal resolution of 4STAR and AERONET observations and the WRF-AAM model outputs, we adapted the model output to match all AERONET and 4STAR observations spatially and temporally to yield the extinction-weighted aerosol age calculated using extinction at 532 nm as in Eq. (1). However, since AERONET does not provide retrievals at 532 nm, we computed the equivalent AOD and SSA at 532 nm to correspond to the model's output using the Ångström formula (Eq. 2) for AOD and the linear interpolation equation for SSA.

2.7 Separating boundary layer (BL) contributions from total column (TC) observations

As sea surface temperatures increase, the boundary layer (BL) deepens offshore before transitioning to a cumulus

regime (Zhang and Zuidema, 2019, 2021; Ryoo et al., 2021). Continental BBA is lofted above 6 km and advected above the cloud layer by free-troposphere (FT) winds (Ryoo et al., 2021), particularly during strong southern African Easterly Jet (AEJ-S) episodes (Adebiyi and Zuidema, 2016). Although generally elevated, subsidence (Wilcox, 2010) and low-level easterlies (Diamond et al., 2018) can entrain BBA into the BL between June and August, altering aerosol properties (Dobracki et al., 2025).

Dang et al. (2022) showed that BBA sampled during ORACLES dominates the FT, while sea salt aerosols may often dominate the BL over the SEA with a fraction of BBA mixed with sea salt aerosols in the BL. Therefore, our goal of investigating the evolution of BBA from TC observations is complicated by the potential contribution of non-BBA from the MBL. To address this and given that AERONET and 4STAR provide columnar retrievals above the observation altitude, we employed a two-pronged approach, detailed in Sects. 2.7.1 and 2.7.2, to isolate the FT aerosol from the columnar observations. First, we applied a model-derived ratio to partition aerosol loading in the FT and BL over the SEA. Subsequently, we implemented a size thresholding technique to exclude contributions from larger particles, ensuring our analysis remains focused on BBA properties.

2.7.1 Application of model-derived extinction ratio

To address the potential influence of MBL aerosol properties on the TC observations by AERONET and 4STAR over the SEA, we use a model-derived vertical distribution of extinction to estimate the FT contributions to the TC measurements, while assuming an external mixing state of particles over the ocean. Specifically, we applied model-derived ratios of extinction in the BL relative to the TC (R_{BL}) and in the FT relative to the TC (R_{FT}) to

i. all AERONET observations at Ascension Island and Namibe and

ii. 4STAR observations when the NASA P-3 aircraft was flying within the BL.

To compute R_{BL} (Eq. 3) and R_{FT}, we applied BLH values from WRF-CAM5 for both sets of observations. The BLH values are estimated according to Chang et al. (2023) and validated with radiosonde observations at Ascension Island (Zhang and Zuidema, 2019).

$$R_{BL} = \frac{\int_{s_{elv}}^{BLH} \beta_{ext}\, dz}{\int_{s_{elv}}^{TOA} \beta_{ext}\, dz} \quad (3)$$

$$R_{FT} = 1 - R_{BL} \quad (4)$$

Using the computed ratios, we partitioned the columnar AOD (AOD_{TC}) measurements at locations (i) and (ii) using the following equations.

$$AOD_{BL} = R_{BL} \times AOD_{TC} \quad (5)$$

$$AOD_{FT} = R_{FT} \times AOD_{TC} \quad (6)$$

Here, AOD_{BL} and AOD_{FT} represent the partial AOD at 532 nm within the BL and FT, respectively. For (i), AOD_{TC} refers to the columnar AOD above the site's elevation and AOD_{BL} represents the portion of AOD between that elevation and the BLH. For (ii), AOD_{TC} refers to the columnar AOD above the P-3 aircraft altitude, while AOD_{BL} represents the portion of AOD between the P-3 flight altitude and the BLH.

We next calculated the proportion of aerosol age and SSA within the FT using the following:

$$Aerosol_{age_{FT}} = \frac{\int_{BLH}^{TOA} \beta_{ext} \times \text{plume age}\, dz}{\int_{BLH}^{TOA} \beta_{ext}\, dz}, \quad (7)$$

$$SSA_{FT} = \frac{(SSA_{TC} \times AOD_{TC}) - (SSA_{BL} \times AOD_{BL})}{AOD_{FT}}. \quad (8)$$

While the WRF-CAM5 BLH values generally agree with observational data, our analysis indicates that the model significantly underestimates aerosol loading in the BL, a limitation also highlighted in prior studies (Figs. 8–11, Doherty et al., 2022). Despite having the most accurate model representation of aerosol properties in the SEA region (Doherty et al., 2022), this underestimation in the BL by WRF-CAM5 (see Figs. S7–S9) affects the representation of BBA properties in the FT at location (i) and (ii) , with physically unrealistic values. To address this, we applied an assumed SSA_{BL} value of 1, recognizing that this introduces a source of uncertainty to the analysis, as it assumes that all aerosols in the BL are purely scattering and does not account for the occasional mixing of BBA with marine sea salt in the BL. To aid the separation of BL and FT BBA, we applied an EAE screening, described below.

2.7.2 Application of extinction Ångström exponent (EAE) thresholds

The extinction Ångström exponent (EAE) is sensitive to the size distribution of aerosol particles (Eck et al., 1999; Schuster et al., 2006; Aladodo et al., 2022). Fine-mode aerosol particles, such as smoke, typically have a higher EAE (usually > 1) than coarse-mode aerosols such as marine sea salt, which typically have a lower EAE (< 1). Along with implementing the model-derived extinction ratio outlined in Sect. 2.7.1, to further discard contributions of other aerosols to the columnar measurements, particularly in atmospheric layers above locations (i) and (ii), we applied an EAE filter. We posit that EAE values < 1 would indicate the presence of sea salt aerosol, whereas EAE values ≥ 1.5 would indicate the dominance of BBA (Eck et al., 1999), while layers with measured EAE values between 1 and 1.5 contain varying degrees of sea salt and BBA following the results of Dang et al.

(2022). We tested four EAE threshold values of ≥ 0.75, ≥ 1, ≥ 1.2, and ≥ 1.4 to successively exclude such measurements, retaining only fine particles while carefully considering the data processing. Our analysis of the EAE thresholding (see Sect. S3 for more details) suggests that EAE of 1.5 for BBA might be applicable near emission sources; lower values during transport and aging led us to choose a lower threshold of 1.2 to have more robust statistics over the ocean.

3 Results and discussion

3.1 Age distribution of smoke plumes

The aerosol age (Fig. 3a) and extinction (Fig. 3b) on 17 October 2018, as derived by the WRF-AAM model, are shown in Fig. 3, with the altitude track of the P-3 aircraft, which flew over the SEA between 07:00–15:00 UTC (see also Fig. S10), overlaid onto the curtain plot. For this case, the model simulates particles at altitudes below 2 km and above 8 km to be substantially older, with plume age ranging from 9–12 d, than those in the mid-FT (3–7 km) with age ranging from 3–8 d. The age of the plume sampled between 12:00–13:00 UTC at the flight intersection with the HYSPLIT trajectory shown in Fig. 1 ranged from 4–8 d relative to HYSPLIT age range of 4–6 d (see Fig. S1 in the Supplement). In Fig. 3b, the vertical distribution of aerosol extinction generally revealed maximum extinction within the lowest 2 km. The model demonstrated a consistent inverse relationship between extinction and height, with extinction decreasing as height increased, reaching a minimum above 6 km.

The modeled vertical distribution of aerosol age and extinction across all ORACLES flight missions and exemplified in Fig. 3 reveals a distinct pattern: aerosols around 7 km, within a central altitude band of 3–8 km, are younger and likely represent aerosols recently transported by the FT jet. In contrast, aerosols below 1 km and above 8 km over the ocean appear to have an older connection to their source regions, suggesting they either followed a different transport route than the FT aerosols or were recirculated by the AEJ-S, as previously described by Adebiyi and Zuidema (2016).

The distribution of aerosol age from all AERONET and 4STAR observations considered in this study (Fig. 4) shows that the oldest BBA is observed near Ascension Island (7.9° S, 14.4° W), a remote island about 2000 km away from the African coast. WRF-AAM outputs predict the samples at Ascension Island to be aged between approximately 7–12 d, with a mean age of approximately 10 d, while for 4STAR observations, WRF-AAM shows that the aerosol age ranged between 3 and 12 d, with a mean age of about 7 d. However, younger BBA was observed over land, closer to the source region of the fires. The plumes sampled at Mongu, Huambo, and Namibe were aged between 1–7 d, 0–6 d, and 3–9 d, respectively, with a mean age of approximately 4, 3.5, and 6 d. The youngest aerosols in the source region were sampled at Huambo (12.8° S, 15.7° E) and Mongu (15.2° S, 23.1° E), with over 75 % of all observations at both stations aged less than 4 d. The mean age of aerosols near the African coast was approximately 6 d, suggesting that the smoke measured at Namibe (15.15° S, 12.17° E) migrated from the primary burning region at Mongu and Huambo. This is further supported by trajectory analysis (see Fig. S1) and by the limited count of active fires recorded in the vicinity of Namibe during the campaign period as shown in Fig. 1. 4STAR observations show a wider age range than those from AERONET sites. This variability is likely attributed to the ORACLES flight strategy, which sometimes targeted freshly emitted smoke from new fires, resulting in the lower age range of 3 to 6 d. The modeled aging pattern suggests the smoke originating from the continent follows a relatively steady trajectory up to Ascension Island. This is supported by HYSPLIT trajectory analysis (see Sect. S2), which reveals that the majority of air masses from the burning region follow a similar path westward, typically reaching Ascension Island within 10 to 12 d.

3.2 Changes in total column SSA with age

Next, we investigate the relationship between SSA and the model-derived age, stratified by the EAE in the TC over the entire study region. We do this by combining the available collocated AERONET, 4STAR, and WRF-AAM output datasets from September 2016, August 2017, and October 2018. Combining data from all three months together provides additional dynamic of change in SSA with time through the burning season months as shown in Eck et al. (2013). The distribution of SSA and EAE by observation site is shown in Fig. 4, while Fig. 5 shows SSA at 532 nm and EAE as a function of model-derived aerosol age for all observations in the TC. The cluster of high-EAE data, seen between 0 and 4 d in Fig. 5, is primarily made up of measurements in the burning region from Mongu and Huambo, with average EAE values of 1.81 and 1.86, respectively (Fig. 4), indicating a dominance of BBA in the TC at these locations. Correspondingly, the TC SSA ranges between 0.77 and 0.97, with a mean TC SSA of 0.86 at the two locations, with over 75 % of the data below 0.90.

The TC SSA result in the source region at Mongu and Huambo implies that fresh BBA (≤ 4 d) is optically dark and highly absorbing of solar radiation as indicated by low SSA values (Table 4), which is consistent with previous findings (Abel et al., 2003; Haywood et al., 2003; Leahy et al., 2007; Eck et al., 2013) in the region. A decrease in TC EAE is observed with increasing distance from the source region (see Fig. S14), indicating larger particle sizes at more remote locations over the SEA. At Namibe, the mean TC EAE is 1.54, with a mean TC SSA of 0.87, ranging from 0.83 to 0.95. This observed trend of increasing particle size aligns with in situ aerosol size measurements (Howes et al., 2023). Aerosols over the SEA exhibit a broad range of TC EAE values, from 0.28 and 2.0, reflecting significant heterogeneity in

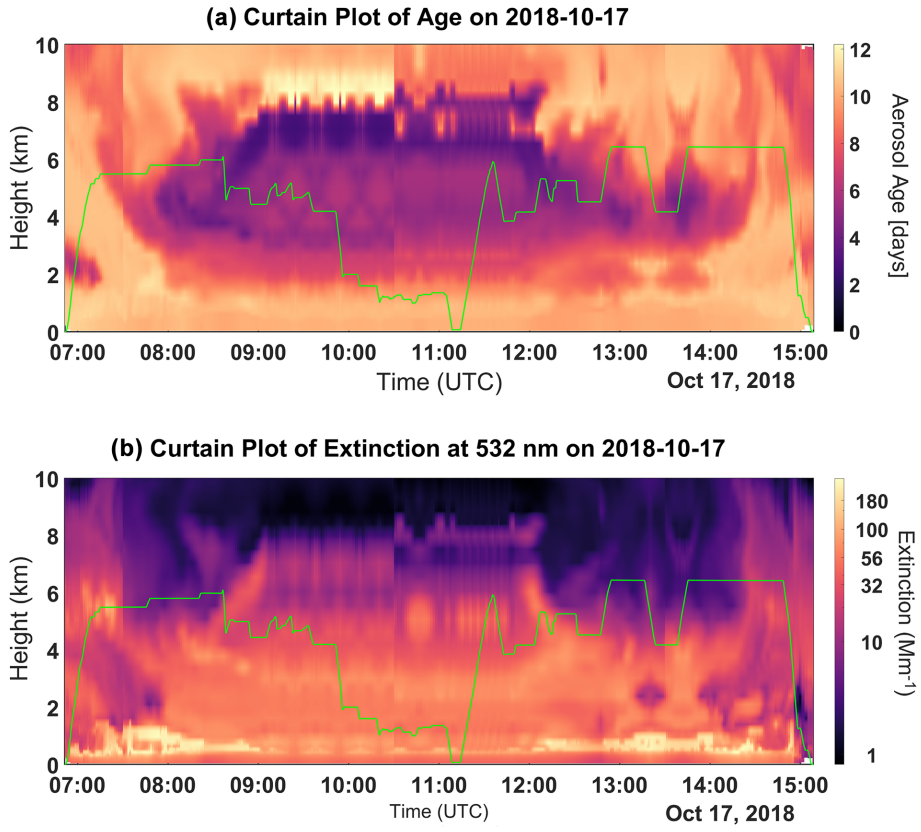

Figure 3. WRF-AAM curtain plot with altitude on the *Y* axis and time in UTC on the *X* axis, showing the smoke plume age forecast **(a)** and aerosol extinction **(b)** along the P-3 track (solid green line) during research flight 10 of the third ORACLES deployment on 17 October 2018. The smoke plume age is calculated as the average of the tracer concentration in each age bin.

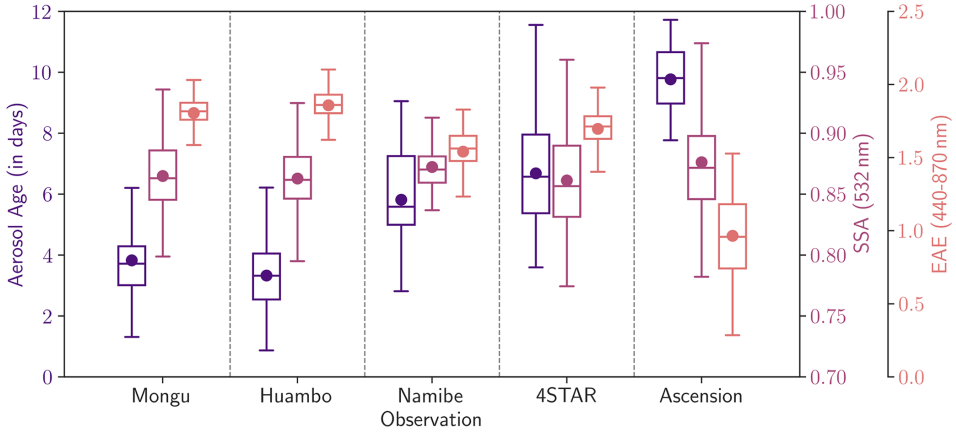

Figure 4. Box and whisker plots showing the distribution of aerosol age (violet), $SSA_{532\,nm}$ (magenta), and EAE (peach) in the TC for available observations at each site. The box–whisker plot shows the 10th (lower whisker), 25th (lower box), 50th (median), 75th (upper box), and 90th (upper whisker) percentiles. The mean value for each parameter is marked with the circle.

particle sizes within the TC. These observations have a mean TC SSA of 0.86 for 4STAR, with a range between 0.67–0.96, and a mean TC SSA of 0.87 at Ascension Island, ranging from 0.78 to 0.99. Some retrievals over the SEA showed both low SSA values (< 0.8) and low EAE values (≤ 1.0), suggesting the possible presence of other aerosol types at Ascension Island (Howes et al., 2023) or a combination of coarse non- or less-absorbing particles and BBA within the same column.

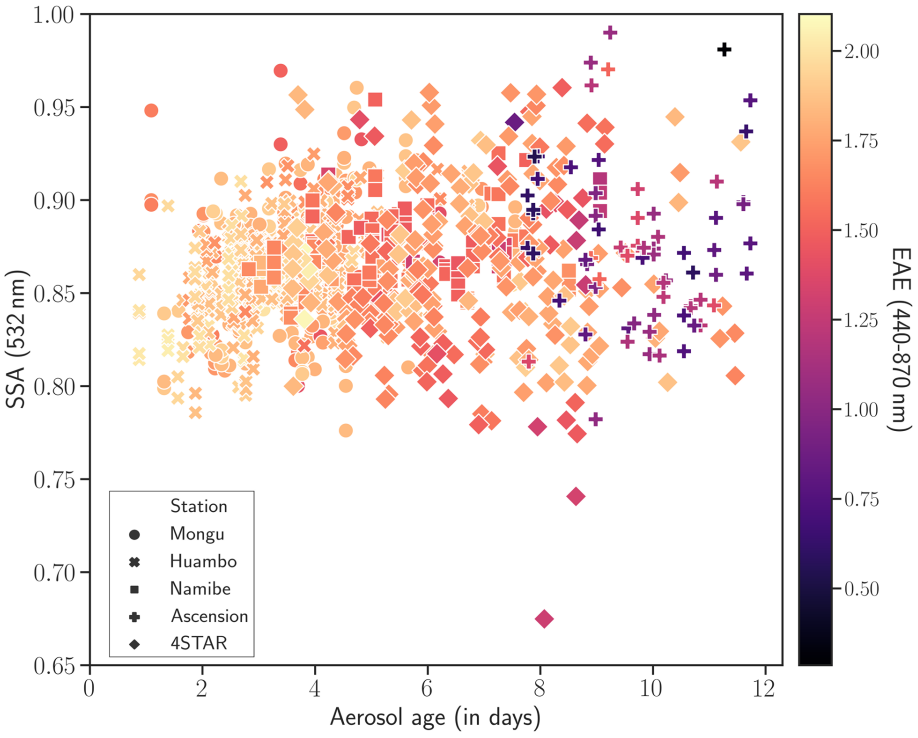

Figure 5. Relationship between $SSA_{532\,nm}$ (y axis), EAE (color bar), and aerosol age (x axis) in the total atmospheric column (TC). The different markers represent the site of observation, while the marker shading represents the EAE.

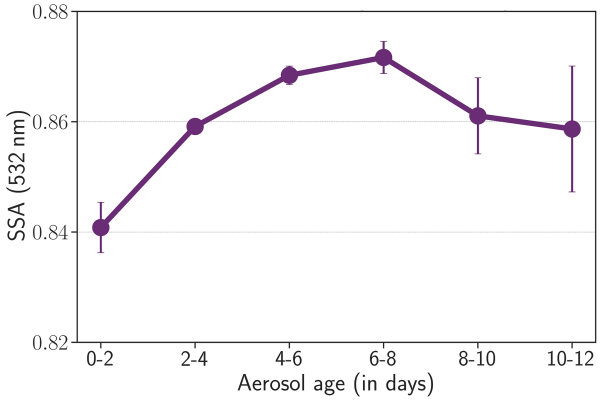

Figure 6. Mean SSA (at 532 nm) within the vertical column (TC SSA) as a function of aerosol age for the optimal threshold (EAE $\geq$ 1.2). Error bars represent the standard error of the mean.

Upon applying an EAE threshold of 1.2 to the TC, we binned the aerosol age into 2 d intervals and estimated the mean TC SSA for each bin (Fig. 6). The result shows that mean TC SSA increases with age, changing from 0.84 within 0 to 2 d of emission over land in the source region to 0.87 after 6 to 8 d, then decreases over the ocean, reaching approximately 0.86 after 10 to 12 d. This result indicates changes in aerosol optical properties during different stages of transport.

3.3 Vertical partitioning of aerosol properties

In this section, we present and analyze the results of the vertical partitioning of aerosol properties, utilizing the model-derived extinction ratio as outlined in Sect. 2.7.1. Through this method, we made comparisons between the optical properties of aerosols residing in the FT and those in the TC, providing insights into the distribution of aerosols across the two layers.

3.3.1 Free-tropospheric aerosol loading

The fraction of AOD in the free troposphere (FT AOD) relative to the total column AOD (TC AOD) over the SEA, derived from the WRF-CAM5 model, is shown in Fig. 7. For AERONET, TC AOD represents the columnar AOD above the site elevation, while for 4STAR, TC AOD refers to the AOD above the aircraft altitude. The modeled FT AOD fraction exhibits considerable spatial variation, with contributions to TC AOD ranging from 0.42 to 0.92 (mean: 0.73) at Ascension Island, 0.68 to 0.99 (mean: 0.95) for 4STAR observations, and 0.70 to 0.95 (mean: 0.86) at Namibe. Only 4STAR sky scans conducted at flight altitudes below the BL top were included in the separation, representing approximately 48 % of the total 4STAR sky scans. The differences in the fraction of FT AOD between Ascension Island, 4STAR, and Namibe (as shown in Fig. 7) can be attributed primarily to the relative proximity to the source regions. The 4STAR

Table 3. Summary statistics of **(a)** the fraction of FT AOD, **(b)** TC AOD and FT AOD, and **(c)** TC EAE and FT EAE.

Site name	Count	Mean	SD	Min	25 %	50 %	75 %	Max
(a) Fraction of FT AOD								
Ascension	69	0.73	0.14	0.42	0.64	0.75	0.85	0.92
Namibe	133	0.86	0.07	0.70	0.82	0.88	0.92	0.95
4STAR	122	0.95	0.05	0.68	0.93	0.97	0.99	0.99
(b) TC AOD (FT AOD) 532 nm								
Ascension	69	0.31 (0.23)	0.15 (0.15)	0.10 (0.08)	0.18 (0.10)	0.28 (0.18)	0.40 (0.33)	0.88 (0.81)
Namibe	133	0.88 (0.76)	0.28 (0.26)	0.47 (0.39)	0.69 (0.54)	0.81 (0.69)	1.04 (0.91)	1.74 (1.58)
4STAR	255	0.36 (0.35)	0.15 (0.15)	0.14 (0.13)	0.24 (0.23)	0.31 (0.30)	0.43 (0.42)	0.85 (0.84)
(c) TC EAE (FT EAE) 440–870 nm								
Ascension	69	0.96 (0.97)	0.27 (0.28)	0.28 (0.28)	0.74 (0.75)	0.96 (0.97)	1.18 (1.20)	1.52 (1.54)
Namibe	133	1.54 (1.55)	0.15 (0.15)	1.01 (1.01)	1.47 (1.47)	1.56 (1.57)	1.64 (1.65)	1.82 (1.83)
4STAR	255	1.69 (1.70)	0.15 (0.15)	0.86 (0.86)	1.63 (1.63)	1.71 (1.71)	1.78 (1.78)	2.08 (2.08)

measurements, taken predominantly east of Ascension Island, captured denser smoke plumes before they reached the island. Additionally, the higher FT AOD in 4STAR compared to AERONET is likely due to unaccounted for AOD between the aircraft altitude and the surface in the 4STAR dataset. This finding emphasizes that a substantial portion of TC AOD, exceeding 50 % on average, resides in the FT, indicating a higher aerosol loading in the FT compared to the MBL over the SEA. Subsequently, the model-derived fraction (Eq. 4) is applied to estimate FT AOD for Ascension Island, 4STAR, and Namibe retrievals using Eq. (6). At Ascension Island, the mean FT AOD for the campaign period is approximately 0.23 compared to the mean TC AOD of 0.31, as shown in Fig. 8 and summarized in Table 3. However, higher mean FT AOD values of 0.35 and 0.76 are observed from 4STAR and at Namibe, respectively. The FT AOD from 4STAR aligns with findings of Shinozuka et al. (2020b), who reported that daytime AOD above cloud is similar to that in clear-sky conditions over the SEA. The observed FT aerosol loading from AERONET and 4STAR measurements over the SEA ocean agrees with the modeled FT AOD reported in Chang et al. (2023) for the same region.

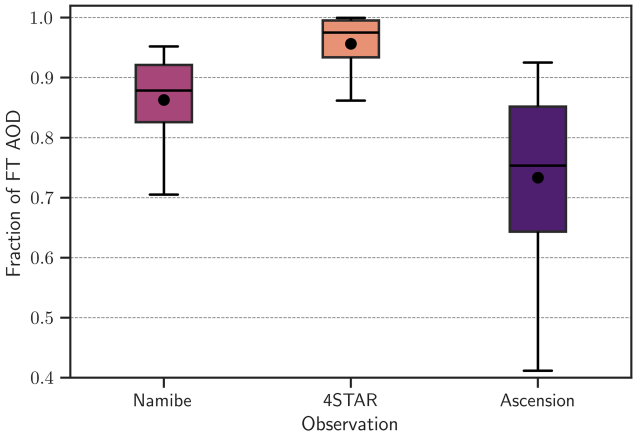

Figure 7. Model-derived fraction of free-tropospheric (FT) AOD to total column (TC) AOD. A fraction of 1 means that aerosol loading is completely in the FT. The box–whisker plot shows the 10th (lower whisker), 25th (lower box), 50th (median), 75th (upper box), and 90th (upper whisker) percentiles of the fraction of FT AOD. The black circle represents the mean fraction. Note that the outliers have been hidden in the figure. Therefore, on average, more than 50 % of the aerosol loading in the ORACLES observation region is in the FT.

3.3.2 Free-tropospheric extinction Ångström exponent

The FT EAE values observed from 4STAR range between approximately 1.0 and 2.1, averaging 1.7, consistent with findings from Leblanc et al. (2020), who reported minimal spatial dependence of above-cloud EAE in the SEA. At Namibe, FT EAE ranges from 1.0–1.82 with a mean of about 1.55.

At Ascension Island, the FT EAE ranges from 0.28 to 1.5 with a mean of approximately 1.0, indicating a variety of particle sizes. The EAE distribution within the FT mirrors the

Table 4. Summary statistics of TC and FT (in parentheses) aerosol age **(a)**, SSA **(b)**, and EAE **(c)** based on observations site.

Site name	Count	Mean	SD	Min	25 %	50 %	75 %	Max
(a) Aerosol age								
Ascension	69	9.77	1.16	7.77	8.99	9.97	10.7	11.73
		(9.68)	(1.32)	(6.98)	(8.45)	(10.02)	(10.69)	(11.73)
Namibe	133	5.82	1.49	2.82	5.00	5.59	7.25	9.05
		(5.23)	(1.55)	(2.59)	(4.08)	(4.78)	(6.73)	(8.55)
Huambo	336	3.33	1.10	0.87	2.54	3.32	4.05	6.80
Mongu	355	3.83	1.25	1.09	3.01	3.72	4.29	7.55
4STAR	255	6.69	1.76	3.60	5.37	6.58	7.96	11.56
		(6.60)	(1.72)	(3.60)	(5.32)	(6.54)	(7.64)	(11.78)
(b) Single-scattering albedo (SSA 532 nm)								
Ascension	69	0.87	0.04	0.78	0.85	0.87	0.90	0.99
		(0.82)	(0.07)	(0.60)	(0.79)	(0.82)	(0.86)	(0.98)
Namibe	133	0.87	0.02	0.83	0.86	0.87	0.88	0.95
		(0.85)	(0.02)	(0.79)	(0.84)	(0.85)	(0.86)	(0.94)
Huambo	336	0.86	0.02	0.78	0.85	0.86	0.88	0.92
Mongu	355	0.86	0.03	0.77	0.84	0.86	0.89	0.97
4STAR	255	0.86	0.04	0.67	0.83	0.85	0.89	0.96
		(0.86)	(0.05)	(0.67)	(0.82)	(0.85)	(0.88)	(0.96)
(c) Extinction Ångström exponent (EAE 440–870 nm)								
Ascension	69	0.96	0.27	0.28	0.74	0.96	1.18	1.52
		(0.97)	(0.28)	(0.28)	(0.75)	(0.97)	(1.20)	(1.54)
Namibe	133	1.54	0.15	1.01	1.47	1.56	1.64	1.82
		(1.55)	(0.15)	(1.01)	(1.47)	(1.57)	(1.65)	(1.83)
Huambo	336	1.86	0.11	0.95	1.80	1.86	1.93	2.10
Mongu	355	1.81	0.11	1.33	1.76	1.81	1.87	2.05
4STAR	255	1.69	0.15	0.86	1.63	1.71	1.78	2.08
		(1.70)	(0.15)	(0.86)	(1.63)	(1.71)	(1.78)	(2.08)

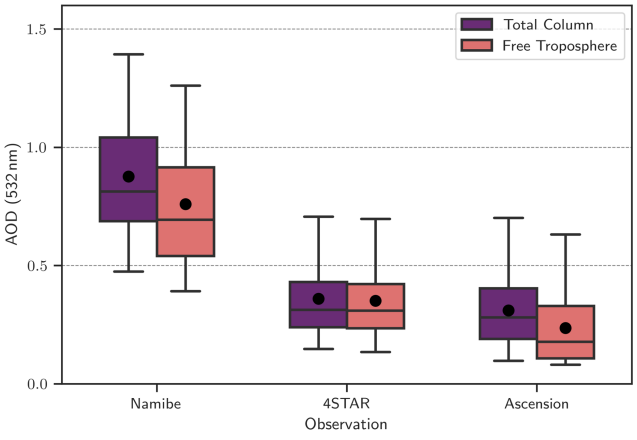

Figure 8. Comparison of AOD (at 532 nm) in the total column (TC) and free troposphere (FT) over the southeast Atlantic (SEA) Ocean. The box–whisker plot shows the 10th (lower whisker), 25th (lower box), 50th (median), 75th (upper box), and 90th (upper whisker) percentiles. Solid black circles represent mean AOD values.

EAE values obtained from the TC, suggesting that the particles' intensive properties remain largely unchanged after isolating MBL contributions. Typically, TC AOD at Ascension that includes the other aerosol contributions would be expected to result in a lower EAE value than the FT AOD-derived value of EAE due to the presence of sea salt aerosols and dimethyl sulfide (DMS) in the maritime environment (Smirnov et al., 2002). However, the lower FT EAE values at Ascension Island suggest there is a source of advected coarse particles in the FT, especially for cases with FT EAE as low as 0.5 shown in Fig. 9. The FT EAE values from 4STAR in the ORACLES campaign region primarily reflect the characteristics of BBA, with mean EAE values greater than 1.2 (Table 3), consistent with previous studies in the region (Pistone et al., 2019; Leblanc et al., 2020).

3.3.3 Free-tropospheric single-scattering albedo

Figure 10 shows the distribution of SSA, EAE, and aerosol age in the free troposphere by observation site. Over the SEA, the FT SSA differs from that of the TC SSA (shown in Fig. 4). At Namibe, the mean FT SSA is 0.85, from a range

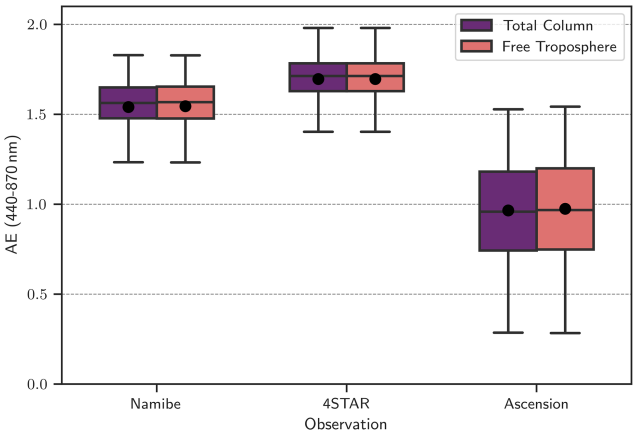

Figure 9. Same as Fig. 8 but for EAE (440–870 nm)

of 0.79–0.94. 4STAR observations show FT SSA values between 0.67–0.96, with a mean of 0.86. At Ascension Island, the FT SSA ranged from 0.60–0.98, with mean of 0.82 (Table 4). These values of FT SSA are lower than TC SSA due to exclusion of the BL portion of the TC, which may include other non-BBA with higher SSA. This difference between FT SSA and TC SSA over the SEA is further discussed in Sect. 3.4. Given that there was no vertical partitioning in the source region since BBA dominates the full column, the FT SSA and TC SSA are equal.

3.4 Evolution of BBA SSA with age in the free troposphere

To further filter out larger particles within the free troposphere, particularly over Ascension Island, we applied a threshold of EAE ≥ 1.2 to the FT dataset, allowing us to focus our analysis on the temporal evolution of FT SSA during BBA-laden episodes. Our findings in Fig. 11 show a progressive increase in mean FT SSA from 0.84 to 0.87 as the aerosols age from 0 to 8 d. After 8 d, FT SSA decreases from 0.87, reaching 0.84 after approximately 12 d of transport. This trend in the mean FT SSA across age bins, summarized in Table 5, begins at 0.84 (0–2 d), increases to 0.857 (2–4 d) and 0.862 (4–6 d), and peaks at 0.871 (6–8 d), before declining to 0.84 (8–10 d) and 0.845 (10–12 d). However, it is important to note the higher uncertainty in FT SSA for the 10–12 d age bin due to the reduced sample size following the EAE filtering (Table 5). We analyzed the contribution of FT SSA from each campaign month to the age bins after filtering (see Tables S1 and S2 in the Supplement).

The analysis showed that for October (2018), there are no observations in the 10–12 d bin and only (3) data points in the 8–10 d bin. In the 8–10 d bin, retrievals are nearly evenly distributed between August (2017) and September (2016), while in the 10–12 d bin, the ratio of September to August retrievals is approximately 3 : 1. The total number (3) of observations from October (2018) in the 8–10 d bin (3) and 10–12 d bin (0) represent less than 2 % of total observations (229) for that year. Meanwhile, the contributions (27) from August (2017) and (42) from September (2016) represent about 5 % and 16 % of the total observations (556 and 258, respectively) for the years. This distribution of observations in the 8–10 and 10–12 d bins suggests that the decrease in SSA observed for older aerosol plumes is not due to an overrepresentation of August data, which climatological studies suggest exhibit lower SSA due to their emissions earlier in the burning season. However, other factors, rather than the timing of the emission, drive the observed SSA change in aged plumes.

The maximum value of mean FT SSA at 6–8 d shows that the BBA absorptivity decreases as the aerosol ages from emission to about 6–8 d. After 6–8 d, the FT SSA decreases, indicating that older BBA is more efficient at absorbing solar radiation. This evolution of FT SSA supports the observations from previous studies where it was reported that the SSA initially increases within a few hours of emission and peaks on the fourth day before decreasing (Sedlacek et al., 2022). The results presented here also support the findings from Dobracki et al. (2023), who showed that in the ORACLES region, SSA decreases as aerosols age because of a reduction in organic aerosol mass concentrations.

We examined the mean FT SSA against the mean TC SSA at the established optimal EAE threshold (Fig. 12) to gain a clearer understanding of the evolution of SSA shown in Fig. 11 and to highlight the significance of employing the combination of the model-based vertical extinction separation with an EAE filter. The results demonstrate that FT SSA decreases by more than 2 % for BBA aged beyond 8 d. This decrease in the mean FT SSA compared to TC SSA suggests that by combining the two methods described in Sect. 2.7, we are able to achieve our desired isolation of fine, BBA particles in the FT from the contribution of larger (EAE < 1.2), non-absorbing aerosols. Applying the EAE filtering solely to the TC data removed larger particles but did not account for other less-absorbing fine particles from mixing of BBA with marine aerosols with the boundary layer (Dang et al., 2022) or non-absorbing fine-mode marine aerosols (Fitzgerald, 1991). However, the application of the EAE filtering to the FT data after partitioning efficiently isolated all non-BBA particles. Overall, the combined use of both techniques reveals a distinct evolution pattern of BBA in the FT. To examine the sensitivity of our assumption that $SSA_{BL} = 1$, we tested alternative SSA_{BL} values to account for varying degrees of absorption within the BL. The results showed an evolution of FT SSA similar to that in Fig. 12, with a decrease in the mean FT SSA after 8 d (Fig. S6).

The changes in SSA presented in this study are primarily associated with chemical and physical processes in the atmosphere (Dobracki et al., 2023). Fresh aerosols over the continent exhibit a low SSA, which we attribute to a high proportion of rBC compared to other aerosol components. This interpretation agrees with previous findings further offshore (Denjean et al., 2020b; Wu et al., 2020; Dobracki et al., 2023)

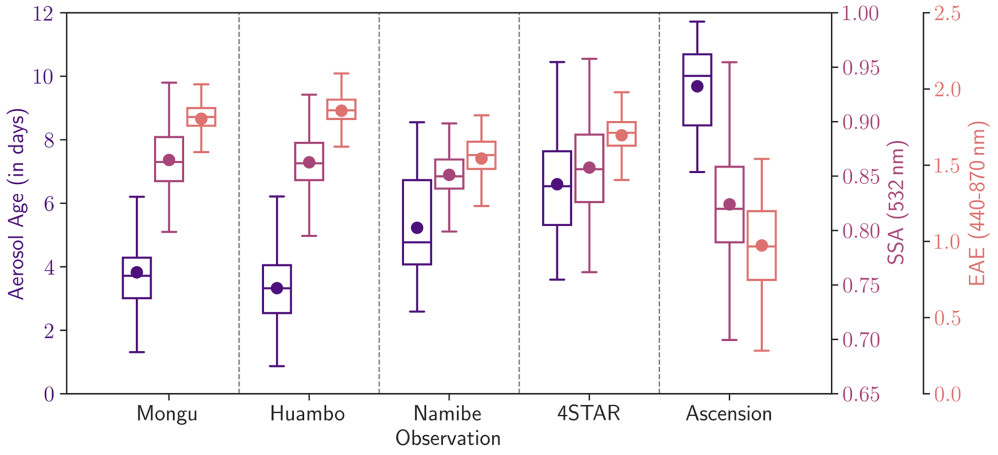

Figure 10. Same as in Fig. 4, but for the free troposphere (FT).

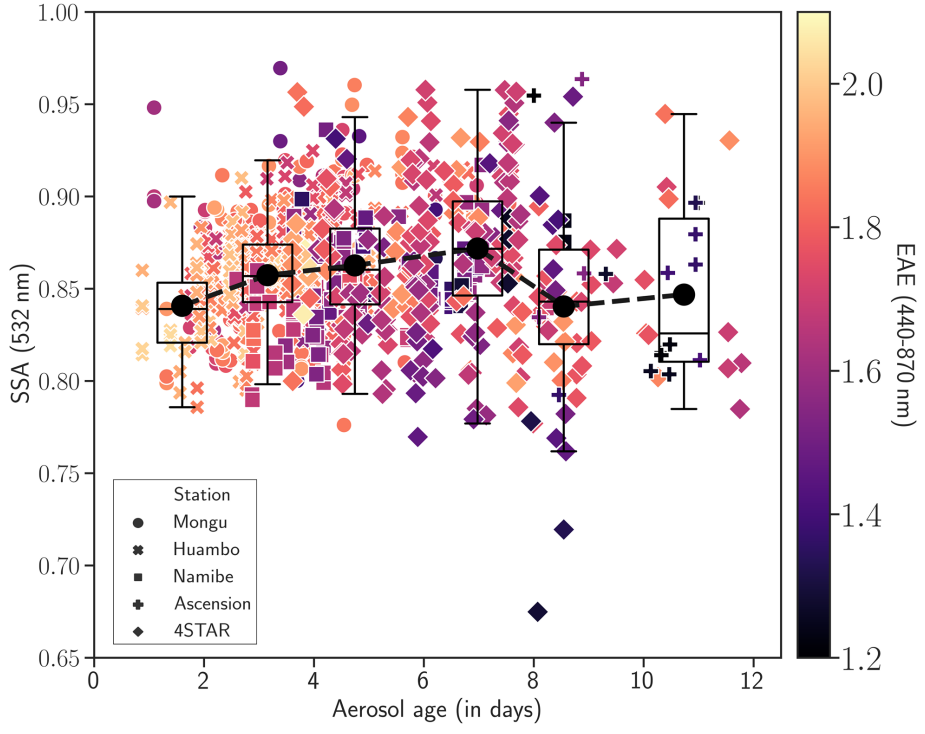

Figure 11. Evolution of FT SSA as a function of aerosol age for the optimal threshold (EAE $\geq$ 1.2). The scatterplot shows the relationship between SSA, EAE, and aerosol age for each observation. The box–whisker plots illustrate the distribution of SSA for the categorized aerosol age bins: [0–2], [2–4], [4–6], [6–8], [8–10], and [10–12], showing the 10th (lower whisker), 25th (lower box), 50th (median), 75th (upper box), and 90th (upper whisker) percentiles. The mean FT SSA for each age bin is represented by the black circles.

and is characteristic of emissions from flaming grassland fires. As these aerosols age in the atmosphere, they accumulate an organic coating, a process that begins rapidly within hours and continues for the first few days (Hodshire et al., 2019; Sedlacek et al., 2022), increasing the contribution of OA to the total mass of the aging particles. Unlike field measurements over the Atlantic Ocean that are relevant for more aged aerosols, our results show a progressive increase in SSA during the first 6 d of aging. After 6–8 d, however, the SSA starts to decrease, consistent with in situ observations over the maritime atmosphere. We hypothesize that this decrease in SSA is due to increased absorption per particle from lensing effects, consistent with Taylor et al. (2020). Moreover, heterogeneous oxidation may drive the repartition of aerosol mass back to the gas phase, reducing the overall OA:BC mass ratio. In addition to compositional changes driven by the ac-

Table 5. Summary statistics of TC SSA and FT SSA (in parentheses) for each age group at EAE ≥ 1.2.

Age group	Count	Mean	SD	Min	25 %	50 %	75 %	Max	SE
0–2	47	0.841	0.03	0.785	0.820	0.840	0.853	0.948	0.004
	(47)	(0.84)	(0.03)	(0.785)	(0.820)	(0.840)	(0.853)	(0.948)	(0.004)
2–4	425	0.859	0.02	0.795	0.845	0.859	0.874	0.960	0.001
	(430)	(0.857)	(0.03)	(0.790)	(0.843)	(0.857)	(0.874)	(0.96)	(0.001)
4–6	319	0.868	0.03	0.776	0.847	0.865	0.887	0.960	0.001
	(327)	(0.862)	(0.03)	(0.769)	(0.841)	(0.860)	(0.882)	(0.960)	(0.001)
6–8	169	0.871	0.04	0.778	0.847	0.873	0.895	0.958	0.003
	(167)	(0.871)	(0.04)	(0.777)	(0.846)	(0.871)	(0.897)	(0.958)	(0.003)
8–10	64	0.861	0.05	0.675	0.829	0.860	0.896	0.970	0.007
	(49)	(0.840)	(0.05)	(0.675)	(0.820)	(0.843)	(0.871)	(0.963)	(0.008)
10–12	16	0.858	0.04	0.802	0.827	0.843	0.901	0.944	0.011
	(23)	(0.845)	(0.04)	(0.785)	(0.810)	(0.825)	(0.890)	(0.944)	(0.009)

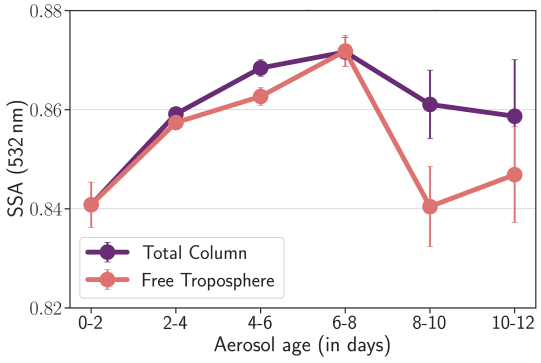

Figure 12. Comparison between the evolution of TC SSA and the evolution of FT SSA for all the aerosol age bins at the optimal threshold (EAE ≥ 1.2). Error bars represent the standard error of the mean.

cumulation and/or evaporation of organic coatings, there is likely a shift in fine-mode particle size, potentially resulting from the same chemical and physical processes that also influence the optical properties.

4 Conclusions

We introduce a novel approach to investigate the evolution of optical properties of BBA during long-range transport from continental southern Africa to the SEA region. This approach integrates ground-based and airborne remote sensing measurements from AERONET and 4STAR, collected during the three ORACLES deployments, with model output from two WRF configurations, WRF-CAM5 and WRF-AAM, to extend the scope for studying aerosol evolution. Our analysis primarily focuses on examining the variations in observed SSA and EAE in relation to the modeled age of the aerosols. This work is unique and builds upon previous research over the SEA by including AERONET observations over land, which allows for a more spatially extensive study of BBA evolution than those prior.

The WRF-AAM model, utilizing CO tracers, provided estimates of the aerosol age (defined as time elapsed since emission). We were able to assess how BBA optical properties evolved during long-range transport over the SEA by tracking the CO tracers in the model for a period of 2 weeks. Our result showed a longitudinal variation in SSA that corresponds to the model-derived aerosol age and aligns with the transport pathway from the continent. The results revealed that SSA generally increased as BBA was transported away from the emission source, with lower SSA values measured at the Mongu and Huambo sites than those measured at the coastal Namibe site. Throughout 2016, 2017, and 2018, there was a clear trend in mean SSA values, generally increasing with distance from the emission source while over land, with low values recorded at Mongu and Huambo, and the highest observed near the central African coast.

We next applied a model-based vertical separation and EAE-based threshold to focus our analysis on the upper-level BBA observations over the SEA. Our analysis showed a distinct temporal trend in FT SSA, where mean FT SSA values initially increased from 0.84 to 0.87 during the first 7 d following emission, followed by a decline back to 0.84 after about 12 d. This implies that the observed aerosol aging led to a 0.03 change in SSA, a trend consistent with in situ measurements reported during the ORACLES campaign by Sedlacek et al. (2022) and Dobracki et al. (2023). In Dobracki et al. (2023), a similar SSA change of approximately 0.06 was observed following a concomitant reduction in OA:BC mass ratio. Given that a variation of ± 0.03 in SSA can result in a difference of up to $\sim 20\,\mathrm{W\,m^{-2}}$ in local direct radiative effect (Wilcox, 2012), the observed SSA changes in our analysis can have substantial effects on Earth's radiative budget, particularly in the SEA, especially considering the influence of BBA above clouds on the sign and magnitude of TOA forcing over dark ocean surface, as noted by Keil and Haywood (2003). To our knowledge, this study is the first to use

remote sensing observations to document changes in BBA properties during long-range transport and associated aging.

We conclude from our analysis that BBA undergoes variations in optical properties that have important implications for the radiation balance. Upon emission, BBA is characterized by low SSA values (high absorptivity) and elevated EAE values, indicating the prevalence of small-sized particles. During initial stages of transport, BBA SSA increases, signifying a reduction in absorptivity, accompanied by a decrease in EAE, indicative of particle growth. However, there is a subsequent decrease in SSA (increase in absorptivity) as BBA continues to age during extended transport. This evolution is driven by atmospheric processes. Dobracki et al. (2023) attributed these changes in SSA to various chemical and physical transformations of BBA in the atmosphere.

These results, in agreement with the findings of Dobracki et al. (2023) and Sedlacek et al. (2022), emphasize the continuous evolution of BBA optical properties, influenced by changes in their chemical and microphysical properties. Accurately capturing these evolving properties throughout their life cycle represents the next step for improving model fidelity and predictive capability. To the best of our knowledge, this study is among the first efforts to investigate BBA evolution over an extended temporal scale, spanning weeks, using columnar observations from remote sensing.

The data analysis techniques and findings from this study contribute to a greater understanding of how BBA optical properties change and the radiative effects associated with those changes. This research also provides further insight into the spatial and temporal evolution of BBA. More importantly, the changes in BBA optical properties associated with aging documented here and elsewhere will need to be incorporated into ESMs to accurately represent BBA aerosol properties and effects and to properly predict future changes in BBA climatic impacts.

Data availability. The NASA P-3 aircraft data were published by the ORACLES Science Team (ORACLES, 2020, https://doi.org/10.5067/SUBORBITAL/ORACLES/DATA001) and can be accessed at the following links. ORACLES-1: https://doi.org/10.5067/Suborbital/ORACLES/P3/2016_V3 (ORACLES, 2021a); ORACLES-2: https://doi.org/10.5067/Suborbital/ORACLES/P3/2017_V3 (ORACLES, 2021b); ORACLES-3: https://doi.org/10.5067/Suborbital/ORACLES/P3/2018_V3 (ORACLES, 2021c). AERONET inversion products are available at https://aeronet.gsfc.nasa.gov/ (NASA, 2025).

Supplement. The supplement related to this article is available online at https://doi.org/10.5194/acp-25-7879-2025-supplement.

Author contributions. This study was conceptualized by JR. JR, CJF, and AAF formulated the methodology. PES and CH ran the WRF simulations and provided model output. KP, SEL, and MSR operated the 4STAR instrument aboard the P-3 aircraft and processed the 4STAR data. LM contributed to the processing of 4STAR retrievals. AAF organized all datasets, performed analyses, and visualized the results. PG and EL are the PIs for AERONET. JR and PZ led efforts to acquire funding and were the PIs for the ORACLES mission. AAF wrote the draft with contributions from all authors.

Competing interests. At least one of the (co-)authors is a member of the editorial board of *Atmospheric Chemistry and Physics*. The peer-review process was guided by an independent editor, and the authors also have no other competing interests to declare.

Disclaimer. Publisher's note: Copernicus Publications remains neutral with regard to jurisdictional claims made in the text, published maps, institutional affiliations, or any other geographical representation in this paper. While Copernicus Publications makes every effort to include appropriate place names, the final responsibility lies with the authors.

Special issue statement. This article is part of the special issue "New observations and related modelling studies of the aerosol–cloud–climate system in the Southeast Atlantic and southern Africa regions (ACP/AMT inter-journal SI)". It is not associated with a conference.

Acknowledgements. Portions of the computational work for this paper were supported by and conducted using resources at the University of Oklahoma (OU) Supercomputing Center for Education & Research (OSCER). We extend our gratitude to the entire NASA ORACLES team for their successful deployment. Our thanks also go to the site PIs and managers for the AERONET stations at Mongu, Huambo, Namibe, and Ascension Island. Data analysis and visualization were carried out using open-source libraries in MATLAB and Python.

Financial support. This research has been supported by the University of Oklahoma (OU) start-up package (grant no. 122007900). The ORACLES field campaign was funded through the NASA Earth Venture Suborbital-2 program (grant no. NNH13ZDA001N-EVS2). Paquita Zuidema acknowledges funding support from DOE ASR award DE-SC0021250.

Review statement. This paper was edited by Quanfu He and reviewed by three anonymous referees.

References

Abel, S. J., Haywood, J. M., Highwood, E. J., Li, J., and Buseck, P. R.: Evolution of biomass burning aerosol properties from an agricultural fire in southern Africa, Geophys. Res. Lett., 30, 1783, https://doi.org/10.1029/2003GL017342, 2003.

Ackerman, A. S., Toon, O. B., Taylor, J. P., Johnson, D. W., Hobbs, P. V., and Ferek, R. J.: Effects of Aerosols on Cloud Albedo: Evaluation of Twomey's Parameterization of Cloud Susceptibility Using Measurements of Ship Tracks, J. Atmos. Sci., 57, 2684–2695, https://doi.org/10.1175/1520-0469(2000)057<2684:Eoaoca>2.0.Co;2, 2000.

Adebiyi, A. A. and Zuidema, P.: The role of the southern African easterly jet in modifying the southeast Atlantic aerosol and cloud environments, Q. J. Roy. Meteor. Soc., 142, 1574–1589, https://doi.org/10.1002/qj.2765, 2016.

Adebiyi, A. A., Zuidema, P., and Abel, S. J.: The Convolution of Dynamics and Moisture with the Presence of Shortwave Absorbing Aerosols over the Southeast Atlantic, J. Climate, 28, 1997–2024, https://doi.org/10.1175/jcli-d-14-00352.1, 2015.

Aladodo, S. S., Akoshile, C. O., Ajibola, T. B., Sani, M., Iborida, O. A., and Fakoya, A. A.: Seasonal Tropospheric Aerosol Classification Using AERONET Spectral Absorption Properties in African Locations, Aerosol Sci. Eng., 6, 246–266, https://doi.org/10.1007/s41810-022-00140-x, 2022.

Albrecht, B. A.: Aerosols, Cloud Microphysics, and Fractional Cloudiness, Science, 245, 1227–1230, https://doi.org/10.1126/science.245.4923.1227, 1989.

Alexander, D. T. L., Crozier, P. A., and Anderson, J. R.: Brown Carbon Spheres in East Asian Outflow and Their Optical Properties, Science, 321, 833–836, https://doi.org/10.1126/science.1155296, 2008.

Andreae, M. O. and Gelencsér, A.: Black carbon or brown carbon? The nature of light-absorbing carbonaceous aerosols, Atmos. Chem. Phys., 6, 3131–3148, https://doi.org/10.5194/acp-6-3131-2006, 2006.

Andreae, M. O. and Rosenfeld, D.: Aerosol–cloud–precipitation interactions. Part 1. The nature and sources of cloud-active aerosols, Earth-Sci. Rev., 89, 13–41, https://doi.org/10.1016/j.earscirev.2008.03.001, 2008.

Baars, H., Radenz, M., Floutsi, A. A., Engelmann, R., Althausen, D., Heese, B., Ansmann, A., Flament, T., Dabas, A., Trapon, D., Reitebuch, O., Bley, S., and Wandinger, U.: Californian Wildfire Smoke Over Europe: A First Example of the Aerosol Observing Capabilities of Aeolus Compared to Ground-Based Lidar, Geophys. Res. Lett., 48, e2020GL092194, https://doi.org/10.1029/2020GL092194, 2021.

Bellouin, N., Quaas, J., Gryspeerdt, E., Kinne, S., Stier, P., Watson-Parris, D., Boucher, O., Carslaw, K. S., Christensen, M., Daniau, A.-L., Dufresne, J.-L., Feingold, G., Fiedler, S., Forster, P., Gettelman, A., Haywood, J. M., Lohmann, U., Malavelle, F., Mauritsen, T., McCoy, D. T., Myhre, G., Mülmenstädt, J., Neubauer, D., Possner, A., Rugenstein, M., Sato, Y., Schulz, M., Schwartz, S. E., Sourdeval, O., Storelvmo, T., Toll, V., Winker, D., and Stevens, B.: Bounding Global Aerosol Radiative Forcing of Climate Change, Rev. Geophys., 58, e2019RG000660, https://doi.org/10.1029/2019RG000660, 2020.

Bergstrom, R. W., Pilewskie, P., Russell, P. B., Redemann, J., Bond, T. C., Quinn, P. K., and Sierau, B.: Spectral absorption properties of atmospheric aerosols, Atmos. Chem. Phys., 7, 5937–5943, https://doi.org/10.5194/acp-7-5937-2007, 2007.

Bond, T. C., Streets, D. G., Yarber, K. F., Nelson, S. M., Woo, J.-H., and Klimont, Z.: A technology-based global inventory of black and organic carbon emissions from combustion, J. Geophys. Res.-Atmos., 109, https://doi.org/10.1029/2003JD003697, 2004.

Bond, T. C., Habib, G., and Bergstrom, R. W.: Limitations in the enhancement of visible light absorption due to mixing state, J. Geophys. Res.-Atmos., 111, D20211, https://doi.org/10.1029/2006JD007315, 2006.

Bond, T. C., Doherty, S. J., Fahey, D. W., Forster, P. M., Berntsen, T., DeAngelo, B. J., Flanner, M. G., Ghan, S., Kärcher, B., Koch, D., Kinne, S., Kondo, Y., Quinn, P. K., Sarofim, M. C., Schultz, M. G., Schulz, M., Venkataraman, C., Zhang, H., Zhang, S., Bellouin, N., Guttikunda, S. K., Hopke, P. K., Jacobson, M. Z., Kaiser, J. W., Klimont, Z., Lohmann, U., Schwarz, J. P., Shindell, D., Storelvmo, T., Warren, S. G., and Zender, C. S.: Bounding the role of black carbon in the climate system: A scientific assessment, J. Geophys. Res.-Atmos., 118, 5380–5552, https://doi.org/10.1002/jgrd.50171, 2013.

Boucher, O.: Atmospheric Aerosols, in: Atmospheric Aerosols: Properties and Climate Impacts, Springer Netherlands, Dordrecht, https://doi.org/10.1007/978-94-017-9649-1_2, 9–24, 2015.

Boucher, O., Randall, D., Artaxo, P., Bretherton, C., Feingold, G., Forster, P., Kerminen, V.-M., Kondo, Y., Liao, H., Lohmann, U., Rasch, P., Satheesh, S., Sherwood, S., Stevens, B., and Zhang, X.: Clouds and Aerosols, in: Climate Change 2013: The Physical Science Basis. Contribution of Working Group I to the Fifth Assessment Report of the Intergovernmental Panel on Climate Change, edited by: IPCC, Cambridge University Press, https://doi.org/10.1017/CBO9781107415324.016., 571–892, 2013.

Bowman, D. M. J. S., Balch, J. K., Artaxo, P., Bond, W. J., Carlson, J. M., Cochrane, M. A., D'Antonio, C. M., DeFries, R. S., Doyle, J. C., Harrison, S. P., Johnston, F. H., Keeley, J. E., Krawchuk, M. A., Kull, C. A., Marston, J. B., Moritz, M. A., Prentice, I. C., Roos, C. I., Scott, A. C., Swetnam, T. W., van der Werf, G. R., and Pyne, S. J.: Fire in the Earth System, Science, 324, 481–484, https://doi.org/10.1126/science.1163886, 2009.

Brown, H., Liu, X., Pokhrel, R., Murphy, S., Lu, Z., Saleh, R., Mielonen, T., Kokkola, H., Bergman, T., Myhre, G., Skeie, R. B., Watson-Paris, D., Stier, P., Johnson, B., Bellouin, N., Schulz, M., Vakkari, V., Beukes, J. P., van Zyl, P. G., Liu, S., and Chand, D.: Biomass burning aerosols in most climate models are too absorbing, Nat. Commun., 12, 277, https://doi.org/10.1038/s41467-020-20482-9, 2021.

Campbell, P., Zhang, Y., Wang, K., Leung, R., Fan, J., Zheng, B., Zhang, Q., and He, K.: Evaluation of a multi-scale WRF-CAM5 simulation during the 2010 East Asian Summer Monsoon, Atmos. Environ., 169, 204–217, https://doi.org/10.1016/j.atmosenv.2017.09.008, 2017.

Chand, D., Wood, R., Anderson, T. L., Satheesh, S. K., and Charlson, R. J.: Satellite-derived direct radiative effect of aerosols dependent on cloud cover, Nat. Geosci., 2, 181–184, https://doi.org/10.1038/ngeo437, 2009.

Chang, I., Gao, L., Flynn, C. J., Shinozuka, Y., Doherty, S. J., Diamond, M. S., Longo, K. M., Ferrada, G. A., Carmichael, G. R.,

Castellanos, P., da Silva, A. M., Saide, P. E., Howes, C., Xue, Z., Mallet, M., Govindaraju, R., Wang, Q., Cheng, Y., Feng, Y., Burton, S. P., Ferrare, R. A., LeBlanc, S. E., Kacenelenbogen, M. S., Pistone, K., Segal-Rozenhaimer, M., Meyer, K. G., Ryoo, J. M., Pfister, L., Adebiyi, A. A., Wood, R., Zuidema, P., Christopher, S. A., and Redemann, J.: On the differences in the vertical distribution of modeled aerosol optical depth over the southeastern Atlantic, Atmos. Chem. Phys., 23, 4283–4309, https://doi.org/10.5194/acp-23-4283-2023, 2023.

Che, H., Stier, P., Gordon, H., Watson-Parris, D., and Deaconu, L.: Cloud adjustments dominate the overall negative aerosol radiative effects of biomass burning aerosols in UKESM1 climate model simulations over the south-eastern Atlantic, Atmos. Chem. Phys., 21, 17–33, https://doi.org/10.5194/acp-21-17-2021, 2021.

Chylek, P. and Wong, J.: Effect of absorbing aerosols on global radiation budget, Geophys. Res. Lett., 22, 929–931, https://doi.org/10.1029/95GL00800, 1995.

Collier, S., Zhou, S., Onasch, T. B., Jaffe, D. A., Kleinman, L., Sedlacek III, A. J., Briggs, N. L., Hee, J., Fortner, E., Shilling, J. E., Worsnop, D., Yokelson, R. J., Parworth, C., Ge, X., Xu, J., Butterfield, Z., Chand, D., Dubey, M. K., Pekour, M. S., Springston, S., and Zhang, Q.: Regional Influence of Aerosol Emissions from Wildfires Driven by Combustion Efficiency: Insights from the BBOP Campaign, Environ. Sci. Technol., 50, 8613–8622, https://doi.org/10.1021/acs.est.6b01617, 2016.

Dang, C., Segal-Rozenhaimer, M., Che, H., Zhang, L., Formenti, P., Taylor, J., Dobracki, A., Purdue, S., Wong, P.-S., Nenes, A., Sedlacek III, A., Coe, H., Redemann, J., Zuidema, P., Howell, S., and Haywood, J.: Biomass burning and marine aerosol processing over the southeast Atlantic Ocean: a TEM single-particle analysis, Atmos. Chem. Phys., 22, 9389–9412, https://doi.org/10.5194/acp-22-9389-2022, 2022.

Darmenov, A. S. and da Silva, A.: The Quick Fire Emissions Dataset (QFED): Documentation of versions 2.1, 2.2 and 2.4, NASA, 2015.

Dedrick, J. L., Russell, L. M., Sedlacek Iii, A. J., Kuang, C., Zawadowicz, M. A., and Lubin, D.: Aerosol-Correlated Cloud Activation for Clean Conditions in the Tropical Atlantic Boundary Layer During LASIC, Geophys. Res. Lett., 51, e2023GL105798, https://doi.org/10.1029/2023GL105798, 2024.

de Graaf, M., Bellouin, N., Tilstra, L. G., Haywood, J., and Stammes, P.: Aerosol direct radiative effect of smoke over clouds over the southeast Atlantic Ocean from 2006 to 2009, Geophys. Res. Lett., 41, 7723–7730, https://doi.org/10.1002/2014GL061103, 2014.

Denjean, C., Bourrianne, T., Burnet, F., Mallet, M., Maury, N., Colomb, A., Dominutti, P., Brito, J., Dupuy, R., Sellegri, K., Schwarzenboeck, A., Flamant, C., and Knippertz, P.: Overview of aerosol optical properties over southern West Africa from DACCIWA aircraft measurements, Atmos. Chem. Phys., 20, 4735–4756, https://doi.org/10.5194/acp-20-4735-2020, 2020a.

Denjean, C., Brito, J., Libois, Q., Mallet, M., Bourrianne, T., Burnet, F., Dupuy, R., Flamant, C., and Knippertz, P.: Unexpected Biomass Burning Aerosol Absorption Enhancement Explained by Black Carbon Mixing State, Geophys. Res. Lett., 47, e2020GL089055, https://doi.org/10.1029/2020GL089055, 2020b.

Diamond, M. S., Dobracki, A., Freitag, S., Small Griswold, J. D., Heikkila, A., Howell, S. G., Kacarab, M. E., Podolske, J. R., Saide, P. E., and Wood, R.: Time-dependent entrainment of smoke presents an observational challenge for assessing aerosol–cloud interactions over the southeast Atlantic Ocean, Atmos. Chem. Phys., 18, 14623–14636, https://doi.org/10.5194/acp-18-14623-2018, 2018.

Dobracki, A., Zuidema, P., Howell, S. G., Saide, P., Freitag, S., Aiken, A. C., Burton, S. P., Sedlacek III, A. J., Redemann, J., and Wood, R.: An attribution of the low single-scattering albedo of biomass burning aerosol over the southeastern Atlantic, Atmos. Chem. Phys., 23, 4775–4799, https://doi.org/10.5194/acp-23-4775-2023, 2023.

Dobracki, A., Lewis, E. R., Sedlacek III, A. J., Tatro, T., Zawadowicz, M. A., and Zuidema, P.: Burning conditions and transportation pathways determine biomass-burning aerosol properties in the Ascension Island marine boundary layer, Atmos. Chem. Phys., 25, 2333–2363, https://doi.org/10.5194/acp-25-2333-2025, 2025.

Doherty, S. J., Saide, P. E., Zuidema, P., Shinozuka, Y., Ferrada, G. A., Gordon, H., Mallet, M., Meyer, K., Painemal, D., Howell, S. G., Freitag, S., Dobracki, A., Podolske, J. R., Burton, S. P., Ferrare, R. A., Howes, C., Nabat, P., Carmichael, G. R., da Silva, A., Pistone, K., Chang, I., Gao, L., Wood, R., and Redemann, J.: Modeled and observed properties related to the direct aerosol radiative effect of biomass burning aerosol over the southeastern Atlantic, Atmos. Chem. Phys., 22, 1–46, https://doi.org/10.5194/acp-22-1-2022, 2022.

Dubovik, O., Holben, B., Eck, T. F., Smirnov, A., Kaufman, Y. J., King, M. D., Tanré, D., and Slutsker, I.: Variability of Absorption and Optical Properties of Key Aerosol Types Observed in Worldwide Locations, J. Atmos. Sci., 59, 590–608, https://doi.org/10.1175/1520-0469(2002)059<0590:Voaaop>2.0.Co;2, 2002.

Dunagan, S. E., Johnson, R., Zavaleta, J., Russell, P. B., Schmid, B., Flynn, C., Redemann, J., Shinozuka, Y., Livingston, J., and Segal-Rosenhaimer, M.: Spectrometer for Sky-Scanning Sun-Tracking Atmospheric Research (4STAR): Instrument Technology, Remote Sens.-Basel, 5, 3872–3895, 2013.

Eck, T. F., Holben, B. N., Reid, J. S., Dubovik, O., Smirnov, A., O'Neill, N. T., Slutsker, I., and Kinne, S.: Wavelength dependence of the optical depth of biomass burning, urban, and desert dust aerosols, J. Geophys. Res.-Atmos., 104, 31333–31349, https://doi.org/10.1029/1999JD900923, 1999.

Eck, T. F., Holben, B. N., Ward, D. E., Mukelabai, M. M., Dubovik, O., Smirnov, A., Schafer, J. S., Hsu, N. C., Piketh, S. J., Queface, A., Roux, J. L., Swap, R. J., and Slutsker, I.: Variability of biomass burning aerosol optical characteristics in southern Africa during the SAFARI 2000 dry season campaign and a comparison of single scattering albedo estimates from radiometric measurements, J. Geophys. Res.-Atmos., 108, 8477, https://doi.org/10.1029/2002JD002321, 2003.

Eck, T. F., Holben, B. N., Reid, J. S., Mukelabai, M. M., Piketh, S. J., Torres, O., Jethva, H. T., Hyer, E. J., Ward, D. E., Dubovik, O., Sinyuk, A., Schafer, J. S., Giles, D. M., Sorokin, M., Smirnov, A., and Slutsker, I.: A seasonal trend of single scattering albedo in southern African biomass-burning particles: Implications for satellite products and estimates of emissions for the world's

largest biomass-burning source, J. Geophys. Res.-Atmos., 118, 6414–6432, https://doi.org/10.1002/jgrd.50500, 2013.

Feng, X., Wang, J., Teng, S., Xu, X., Zhu, B., Wang, J., Zhu, X., Yurkin, M. A., and Liu, C.: Can light absorption of black carbon still be enhanced by mixing with absorbing materials?, Atmos. Environ., 253, 118358, https://doi.org/10.1016/j.atmosenv.2021.118358, 2021.

Feng, Y., Ramanathan, V., and Kotamarthi, V. R.: Brown carbon: a significant atmospheric absorber of solar radiation?, Atmos. Chem. Phys., 13, 8607–8621, https://doi.org/10.5194/acp-13-8607-2013, 2013.

Fitzgerald, J. W.: Marine aerosols: A review, Atmos. Environ. A-Gen., 25, 533–545, https://doi.org/10.1016/0960-1686(91)90050-H, 1991.

Formenti, P., D'Anna, B., Flamant, C., Mallet, M., Piketh, S. J., Schepanski, K., Waquet, F., Auriol, F., Brogniez, G., Burnet, F., Chaboureau, J.-P., Chauvigné, A., Chazette, P., Denjean, C., Desboeufs, K., Doussin, J.-F., Elguindi, N., Feuerstein, S., Gaetani, M., Giorio, C., Klopper, D., Mallet, M. D., Nabat, P., Monod, A., Solmon, F., Namwoonde, A., Chikwililwa, C., Mushi, R., Welton, E. J., and Holben, B.: The Aerosols, Radiation and Clouds in Southern Africa Field Campaign in Namibia: Overview, Illustrative Observations, and Way Forward, B. Am. Meteorol. Soc., 100, 1277–1298, https://doi.org/10.1175/bams-d-17-0278.1, 2019.

Giles, D. M., Sinyuk, A., Sorokin, M. G., Schafer, J. S., Smirnov, A., Slutsker, I., Eck, T. F., Holben, B. N., Lewis, J. R., Campbell, J. R., Welton, E. J., Korkin, S. V., and Lyapustin, A. I.: Advancements in the Aerosol Robotic Network (AERONET) Version 3 database – automated near-real-time quality control algorithm with improved cloud screening for Sun photometer aerosol optical depth (AOD) measurements, Atmos. Meas. Tech., 12, 169–209, https://doi.org/10.5194/amt-12-169-2019, 2019.

Granier, C., Bessagnet, B., Bond, T., D'Angiola, A., Denier van der Gon, H., Frost, G. J., Heil, A., Kaiser, J. W., Kinne, S., Klimont, Z., Kloster, S., Lamarque, J.-F., Liousse, C., Masui, T., Meleux, F., Mieville, A., Ohara, T., Raut, J.-C., Riahi, K., Schultz, M. G., Smith, S. J., Thompson, A., van Aardenne, J., van der Werf, G. R., and van Vuuren, D. P.: Evolution of anthropogenic and biomass burning emissions of air pollutants at global and regional scales during the 1980–2010 period, Climatic Change, 109, 163, https://doi.org/10.1007/s10584-011-0154-1, 2011.

Grell, G. A., Peckham, S. E., Schmitz, R., McKeen, S. A., Frost, G., Skamarock, W. C., and Eder, B.: Fully coupled "online" chemistry within the WRF model, Atmos. Environ., 39, 6957–6975, https://doi.org/10.1016/j.atmosenv.2005.04.027, 2005.

Hansen, J., Sato, M., and Ruedy, R.: Radiative forcing and climate response, J. Geophys. Res.-Atmos., 102, 6831–6864, https://doi.org/10.1029/96JD03436, 1997.

Haywood, J. M. and Shine, K. P.: Multi-spectral calculations of the direct radiative forcing of tropospheric sulphate and soot aerosols using a column model, Q. J. Roy. Meteor. Soc., 123, 1907–1930, https://doi.org/10.1002/qj.49712354307, 1997.

Haywood, J. M., Osborne, S. R., Francis, P. N., Keil, A., Formenti, P., Andreae, M. O., and Kaye, P. H.: The mean physical and optical properties of regional haze dominated by biomass burning aerosol measured from the C-130 aircraft during SAFARI 2000, J. Geophys. Res.-Atmos., 108, 8473, https://doi.org/10.1029/2002JD002226, 2003.

Haywood, J. M., Abel, S. J., Barrett, P. A., Bellouin, N., Blyth, A., Bower, K. N., Brooks, M., Carslaw, K., Che, H., Coe, H., Cotterell, M. I., Crawford, I., Cui, Z., Davies, N., Dingley, B., Field, P., Formenti, P., Gordon, H., de Graaf, M., Herbert, R., Johnson, B., Jones, A. C., Langridge, J. M., Malavelle, F., Partridge, D. G., Peers, F., Redemann, J., Stier, P., Szpek, K., Taylor, J. W., Watson-Parris, D., Wood, R., Wu, H., and Zuidema, P.: The CLoud–Aerosol–Radiation Interaction and Forcing: Year 2017 (CLARIFY-2017) measurement campaign, Atmos. Chem. Phys., 21, 1049–1084, https://doi.org/10.5194/acp-21-1049-2021, 2021.

Hodshire, A. L., Akherati, A., Alvarado, M. J., Brown-Steiner, B., Jathar, S. H., Jimenez, J. L., Kreidenweis, S. M., Lonsdale, C. R., Onasch, T. B., Ortega, A. M., and Pierce, J. R.: Aging Effects on Biomass Burning Aerosol Mass and Composition: A Critical Review of Field and Laboratory Studies, Environ. Sci. Technol., 53, 10007–10022, https://doi.org/10.1021/acs.est.9b02588, 2019.

Holanda, B. A., Pöhlker, M. L., Walter, D., Saturno, J., Sörgel, M., Ditas, J., Ditas, F., Schulz, C., Franco, M. A., Wang, Q., Donth, T., Artaxo, P., Barbosa, H. M. J., Borrmann, S., Braga, R., Brito, J., Cheng, Y., Dollner, M., Kaiser, J. W., Klimach, T., Knote, C., Krüger, O. O., Fütterer, D., Lavrič, J. V., Ma, N., Machado, L. A. T., Ming, J., Morais, F. G., Paulsen, H., Sauer, D., Schlager, H., Schneider, J., Su, H., Weinzierl, B., Walser, A., Wendisch, M., Ziereis, H., Zöger, M., Pöschl, U., Andreae, M. O., and Pöhlker, C.: Influx of African biomass burning aerosol during the Amazonian dry season through layered transatlantic transport of black carbon-rich smoke, Atmos. Chem. Phys., 20, 4757–4785, https://doi.org/10.5194/acp-20-4757-2020, 2020.

Holben, B. N., Eck, T. F., Slutsker, I., Tanré, D., Buis, J. P., Setzer, A., Vermote, E., Reagan, J. A., Kaufman, Y. J., Nakajima, T., Lavenu, F., Jankowiak, I., and Smirnov, A.: AERONET—A Federated Instrument Network and Data Archive for Aerosol Characterization, Remote Sens. Environ., 66, 1–16, https://doi.org/10.1016/S0034-4257(98)00031-5, 1998.

Hopkins, R. J., Lewis, K., Desyaterik, Y., Wang, Z., Tivanski, A. V., Arnott, W. P., Laskin, A., and Gilles, M. K.: Correlations between optical, chemical and physical properties of biomass burn aerosols, Geophys. Res. Lett., 34, L18806, https://doi.org/10.1029/2007GL030502, 2007.

Howes, C., Saide, P. E., Coe, H., Dobracki, A., Freitag, S., Haywood, J. M., Howell, S. G., Gupta, S., Uin, J., Kacarab, M., Kuang, C., Leung, L. R., Nenes, A., McFarquhar, G. M., Podolske, J., Redemann, J., Sedlacek, A. J., Thornhill, K. L., Wong, J. P. S., Wood, R., Wu, H., Zhang, Y., Zhang, J., and Zuidema, P.: Biomass-burning smoke's properties and its interactions with marine stratocumulus clouds in WRF-CAM5 and southeastern Atlantic field campaigns, Atmos. Chem. Phys., 23, 13911–13940, https://doi.org/10.5194/acp-23-13911-2023, 2023.

Jen, C. N., Hatch, L. E., Selimovic, V., Yokelson, R. J., Weber, R., Fernandez, A. E., Kreisberg, N. M., Barsanti, K. C., and Goldstein, A. H.: Speciated and total emission factors of particulate organics from burning western US wildland fuels and their dependence on combustion efficiency, Atmos. Chem. Phys., 19, 1013–1026, https://doi.org/10.5194/acp-19-1013-2019, 2019.

Jimenez, J. L., Canagaratna, M. R., Donahue, N. M., Prevot, A. S. H., Zhang, Q., Kroll, J. H., DeCarlo, P. F., Allan, J. D., Coe,

H., Ng, N. L., Aiken, A. C., Docherty, K. S., Ulbrich, I. M., Grieshop, A. P., Robinson, A. L., Duplissy, J., Smith, J. D., Wilson, K. R., Lanz, V. A., Hueglin, C., Sun, Y. L., Tian, J., Laaksonen, A., Raatikainen, T., Rautiainen, J., Vaattovaara, P., Ehn, M., Kulmala, M., Tomlinson, J. M., Collins, D. R., Cubison, M. J., E., Dunlea, J., Huffman, J. A., Onasch, T. B., Alfarra, M. R., Williams, P. I., Bower, K., Kondo, Y., Schneider, J., Drewnick, F., Borrmann, S., Weimer, S., Demerjian, K., Salcedo, D., Cottrell, L., Griffin, R., Takami, A., Miyoshi, T., Hatakeyama, S., Shimono, A., Sun, J. Y., Zhang, Y. M., Dzepina, K., Kimmel, J. R., Sueper, D., Jayne, J. T., Herndon, S. C., Trimborn, A. M., Williams, L. R., Wood, E. C., Middlebrook, A. M., Kolb, C. E., Baltensperger, U., and Worsnop, D. R.: Evolution of Organic Aerosols in the Atmosphere, Science, 326, 1525–1529, https://doi.org/10.1126/science.1180353, 2009.

Jones, M. W., Abatzoglou, J. T., Veraverbeke, S., Andela, N., Lasslop, G., Forkel, M., Smith, A. J. P., Burton, C., Betts, R. A., van der Werf, G. R., Sitch, S., Canadell, J. G., Santín, C., Kolden, C., Doerr, S. H., and Le Quéré, C.: Global and Regional Trends and Drivers of Fire Under Climate Change, Rev. Geophys., 60, e2020RG000726, https://doi.org/10.1029/2020RG000726, 2022.

Keil, A. and Haywood, J. M.: Solar radiative forcing by biomass burning aerosol particles during SAFARI 2000: A case study based on measured aerosol and cloud properties, J. Geophys. Res.-Atmos., 108, 8467, https://doi.org/10.1029/2002JD002315, 2003.

Keywood, M., Kanakidou, M., Stohl, A., Dentener, F., Grassi, G., Meyer, C. P., Torseth, K., Edwards, D., Thompson, A. M., Lohmann, U., and Burrows, J.: Fire in the Air: Biomass Burning Impacts in a Changing Climate, Crit. Rev. Env. Sci. Tec., 43, 40–83, https://doi.org/10.1080/10643389.2011.604248, 2013.

Kleinman, L. I., Sedlacek III, A. J., Adachi, K., Buseck, P. R., Collier, S., Dubey, M. K., Hodshire, A. L., Lewis, E., Onasch, T. B., Pierce, J. R., Shilling, J., Springston, S. R., Wang, J., Zhang, Q., Zhou, S., and Yokelson, R. J.: Rapid evolution of aerosol particles and their optical properties downwind of wildfires in the western US, Atmos. Chem. Phys., 20, 13319–13341, https://doi.org/10.5194/acp-20-13319-2020, 2020.

Koch, D. and Del Genio, A. D.: Black carbon semi-direct effects on cloud cover: review and synthesis, Atmos. Chem. Phys., 10, 7685–7696, https://doi.org/10.5194/acp-10-7685-2010, 2010.

Konovalov, I. B., Golovushkin, N. A., Beekmann, M., and Andreae, M. O.: Insights into the aging of biomass burning aerosol from satellite observations and 3D atmospheric modeling: evolution of the aerosol optical properties in Siberian wildfire plumes, Atmos. Chem. Phys., 21, 357–392, https://doi.org/10.5194/acp-21-357-2021, 2021.

Lack, D. A. and Cappa, C. D.: Impact of brown and clear carbon on light absorption enhancement, single scatter albedo and absorption wavelength dependence of black carbon, Atmos. Chem. Phys., 10, 4207–4220, https://doi.org/10.5194/acp-10-4207-2010, 2010.

Laskin, A., Laskin, J., and Nizkorodov, S. A.: Chemistry of Atmospheric Brown Carbon, Chem. Rev., 115, 4335–4382, https://doi.org/10.1021/cr5006167, 2015.

Leahy, L. V., Anderson, T. L., Eck, T. F., and Bergstrom, R. W.: A synthesis of single scattering albedo of biomass burning aerosol over southern Africa during SAFARI 2000, Geophys. Res. Lett., 34, L12814, https://doi.org/10.1029/2007GL029697, 2007.

LeBlanc, S. E., Redemann, J., Flynn, C., Pistone, K., Kacenelenbogen, M., Segal-Rosenheimer, M., Shinozuka, Y., Dunagan, S., Dahlgren, R. P., Meyer, K., Podolske, J., Howell, S. G., Freitag, S., Small-Griswold, J., Holben, B., Diamond, M., Wood, R., Formenti, P., Piketh, S., Maggs-Kölling, G., Gerber, M., and Namwoonde, A.: Above-cloud aerosol optical depth from airborne observations in the southeast Atlantic, Atmos. Chem. Phys., 20, 1565–1590, https://doi.org/10.5194/acp-20-1565-2020, 2020.

Lenhardt, E. D., Gao, L., Redemann, J., Xu, F., Burton, S. P., Cairns, B., Chang, I., Ferrare, R. A., Hostetler, C. A., Saide, P. E., Howes, C., Shinozuka, Y., Stamnes, S., Kacarab, M., Dobracki, A., Wong, J., Freitag, S., and Nenes, A.: Use of lidar aerosol extinction and backscatter coefficients to estimate cloud condensation nuclei (CCN) concentrations in the southeast Atlantic, Atmos. Meas. Tech., 16, 2037–2054, https://doi.org/10.5194/amt-16-2037-2023, 2023.

Levin, E. J. T., McMeeking, G. R., Carrico, C. M., Mack, L. E., Kreidenweis, S. M., Wold, C. E., Moosmüller, H., Arnott, W. P., Hao, W. M., Collett Jr., J. L., and Malm, W. C.: Biomass burning smoke aerosol properties measured during Fire Laboratory at Missoula Experiments (FLAME), J. Geophys. Res.-Atmos., 115, D18210, https://doi.org/10.1029/2009JD013601, 2010.

Liu, D., Li, S., Hu, D., Kong, S., Cheng, Y., Wu, Y., Ding, S., Hu, K., Zheng, S., Yan, Q., Zheng, H., Zhao, D., Tian, P., Ye, J., Huang, M., and Ding, D.: Evolution of Aerosol Optical Properties from Wood Smoke in Real Atmosphere Influenced by Burning Phase and Solar Radiation, Environ. Sci. Technol., 55, 5677–5688, https://doi.org/10.1021/acs.est.0c07569, 2021.

Liu, S., Aiken, A. C., Arata, C., Dubey, M. K., Stockwell, C. E., Yokelson, R. J., Stone, E. A., Jayarathne, T., Robinson, A. L., DeMott, P. J., and Kreidenweis, S. M.: Aerosol single scattering albedo dependence on biomass combustion efficiency: Laboratory and field studies, Geophys. Res. Lett., 41, 742–748, https://doi.org/10.1002/2013gl058392, 2014.

Ma, P.-L., Rasch, P. J., Fast, J. D., Easter, R. C., Gustafson Jr., W. I., Liu, X., Ghan, S. J., and Singh, B.: Assessing the CAM5 physics suite in the WRF-Chem model: implementation, resolution sensitivity, and a first evaluation for a regional case study, Geosci. Model Dev., 7, 755–778, https://doi.org/10.5194/gmd-7-755-2014, 2014.

Mallet, M., Solmon, F., Nabat, P., Elguindi, N., Waquet, F., Bouniol, D., Sayer, A. M., Meyer, K., Roehrig, R., Michou, M., Zuidema, P., Flamant, C., Redemann, J., and Formenti, P.: Direct and semi-direct radiative forcing of biomass-burning aerosols over the southeast Atlantic (SEA) and its sensitivity to absorbing properties: a regional climate modeling study, Atmos. Chem. Phys., 20, 13191–13216, https://doi.org/10.5194/acp-20-13191-2020, 2020.

Meyer, K., Platnick, S., Oreopoulos, L., and Lee, D.: Estimating the direct radiative effect of absorbing aerosols overlying marine boundary layer clouds in the southeast Atlantic using MODIS and CALIOP, J. Geophys. Res.-Atmos., 118, 4801–4815, https://doi.org/10.1002/jgrd.50449, 2013.

Mishra, A. K., Koren, I., and Rudich, Y.: Effect of aerosol vertical distribution on aerosol-radiation interaction: A theoretical prospect, Heliyon, 1, e00036, https://doi.org/10.1016/j.heliyon.2015.e00036, 2015.

Mitchell, L. T., Redemann, J., Pistone, K., LeBlanc, S., and Schmidt, S.: Subseasonal and Spatial Variability of Biomass Burning Aerosol Radiative Properties Observed over the Southeast Atlantic during ORACLES 2016–2018 by 4STAR, In-Situ, and the Southern African AERONET Extended Record, in: AGU23, 11–15 December 2023, San Francisco, CA2023, 2023.

Moosmüller, H., Engelbrecht, J. P., Skiba, M., Frey, G., Chakrabarty, R. K., and Arnott, W. P.: Single scattering albedo of fine mineral dust aerosols controlled by iron concentration, J. Geophys. Res.-Atmos., 117, D11210, https://doi.org/10.1029/2011JD016909, 2012.

NASA: AERONET, https://aeronet.gsfc.nasa.gov/ (last access: 15 July 2025), 2025.

Nascimento, J. P., Bela, M. M., Meller, B. B., Banducci, A. L., Rizzo, L. V., Vara-Vela, A. L., Barbosa, H. M. J., Gomes, H., Rafee, S. A. A., Franco, M. A., Carbone, S., Cirino, G. G., Souza, R. A. F., McKeen, S. A., and Artaxo, P.: Aerosols from anthropogenic and biogenic sources and their interactions – modeling aerosol formation, optical properties, and impacts over the central Amazon basin, Atmos. Chem. Phys., 21, 6755–6779, https://doi.org/10.5194/acp-21-6755-2021, 2021.

ORACLES – ORACLES Science Team: ObseRvations of Aerosols above CLouds and their intEractionS, ORACLES [data set], https://doi.org/10.5067/SUBORBITAL/ORACLES/DATA001F, 2020.

ORACLES – ORACLES Science Team: ORACLES-1 P3 Instrument Suite (V3) Details, ORACLES [data set], https://doi.org/10.5067/Suborbital/ORACLES/P3/2016_V3, 2021a.

ORACLES – ORACLES Science Team: ORACLES-2 P3 Instrument Suite (V3) Details, ORACLES [data set], https://doi.org/10.5067/Suborbital/ORACLES/P3/2017_V3, 2021b.

ORACLES:– ORACLES Science Team: ORACLES-3 P3 Instrument Suite (V3) Details, ORACLES [data set], https://doi.org/10.5067/Suborbital/ORACLES/P3/2018_V3, 2021c.

Pistone, K., Redemann, J., Doherty, S., Zuidema, P., Burton, S., Cairns, B., Cochrane, S., Ferrare, R., Flynn, C., Freitag, S., Howell, S. G., Kacenelenbogen, M., LeBlanc, S., Liu, X., Schmidt, K. S., Sedlacek III, A. J., Segal-Rozenhaimer, M., Shinozuka, Y., Stamnes, S., van Diedenhoven, B., Van Harten, G., and Xu, F.: Intercomparison of biomass burning aerosol optical properties from in situ and remote-sensing instruments in ORACLES-2016, Atmos. Chem. Phys., 19, 9181–9208, https://doi.org/10.5194/acp-19-9181-2019, 2019.

Queface, A. J., Piketh, S. J., Eck, T. F., Tsay, S.-C., and Mavume, A. F.: Climatology of aerosol optical properties in Southern Africa, Atmos. Environ., 45, 2910–2921, https://doi.org/10.1016/j.atmosenv.2011.01.056, 2011.

Redemann, J., Russell, P. B., and Hamill, P.: Dependence of aerosol light absorption and single-scattering albedo on ambient relative humidity for sulfate aerosols with black carbon cores, J. Geophys. Res.-Atmos., 106, 27485–27495, https://doi.org/10.1029/2001JD900231, 2001.

Redemann, J., Wood, R., Zuidema, P., Doherty, S. J., Luna, B., LeBlanc, S. E., Diamond, M. S., Shinozuka, Y., Chang, I. Y., Ueyama, R., Pfister, L., Ryoo, J.-M., Dobracki, A. N., da Silva, A. M., Longo, K. M., Kacenelenbogen, M. S., Flynn, C. J., Pistone, K., Knox, N. M., Piketh, S. J., Haywood, J. M., Formenti, P., Mallet, M., Stier, P., Ackerman, A. S., Bauer, S. E., Fridlind, A. M., Carmichael, G. R., Saide, P. E., Ferrada, G. A., Howell, S. G., Freitag, S., Cairns, B., Holben, B. N., Knobelspiesse, K. D., Tanelli, S., L'Ecuyer, T. S., Dzambo, A. M., Sy, O. O., McFarquhar, G. M., Poellot, M. R., Gupta, S., O'Brien, J. R., Nenes, A., Kacarab, M., Wong, J. P. S., Small-Griswold, J. D., Thornhill, K. L., Noone, D., Podolske, J. R., Schmidt, K. S., Pilewskie, P., Chen, H., Cochrane, S. P., Sedlacek, A. J., Lang, T. J., Stith, E., Segal-Rozenhaimer, M., Ferrare, R. A., Burton, S. P., Hostetler, C. A., Diner, D. J., Seidel, F. C., Platnick, S. E., Myers, J. S., Meyer, K. G., Spangenberg, D. A., Maring, H., and Gao, L.: An overview of the ORACLES (ObseRvations of Aerosols above CLouds and their intEractionS) project: aerosol–cloud–radiation interactions in the southeast Atlantic basin, Atmos. Chem. Phys., 21, 1507–1563, https://doi.org/10.5194/acp-21-1507-2021, 2021.

Reid, J. S., Hobbs, P. V., Ferek, R. J., Blake, D. R., Martins, J. V., Dunlap, M. R., and Liousse, C.: Physical, chemical, and optical properties of regional hazes dominated by smoke in Brazil, J. Geophys. Res.-Atmos., 103, 32059–32080, https://doi.org/10.1029/98JD00458, 1998.

Ryoo, J.-M., Pfister, L., Ueyama, R., Zuidema, P., Wood, R., Chang, I., and Redemann, J.: A meteorological overview of the ORACLES (ObseRvations of Aerosols above CLouds and their intEractionS) campaign over the southeastern Atlantic during 2016–2018: Part 1 – Climatology, Atmos. Chem. Phys., 21, 16689–16707, https://doi.org/10.5194/acp-21-16689-2021, 2021.

Saide, P. E., Thompson, G., Eidhammer, T., da Silva, A. M., Pierce, R. B., and Carmichael, G. R.: Assessment of biomass burning smoke influence on environmental conditions for multi-year tornado outbreaks by combining aerosol-aware microphysics and fire emission constraints, J. Geophys. Res.-Atmos., 121, 10294–10311, https://doi.org/10.1002/2016JD025056, 2016.

Sakaeda, N., Wood, R., and Rasch, P. J.: Direct and semidirect aerosol effects of southern African biomass burning aerosol, J. Geophys. Res.-Atmos., 116, D12205, https://doi.org/10.1029/2010JD015540, 2011.

Saleh, R., Marks, M., Heo, J., Adams, P. J., Donahue, N. M., and Robinson, A. L.: Contribution of brown carbon and lensing to the direct radiative effect of carbonaceous aerosols from biomass and biofuel burning emissions, J. Geophys. Res.-Atmos., 120, 10,285-210,296, https://doi.org/10.1002/2015JD023697, 2015.

Samset, B. H., Stjern, C. W., Andrews, E., Kahn, R. A., Myhre, G., Schulz, M., and Schuster, G. L.: Aerosol Absorption: Progress Towards Global and Regional Constraints, Current Climate Change Reports, 4, 65–83, https://doi.org/10.1007/s40641-018-0091-4, 2018.

Santer, B. D., Taylor, K. E., Wigley, T. M. L., Johns, T. C., Jones, P. D., Karoly, D. J., Mitchell, J. F. B., Oort, A. H., Penner, J. E., Ramaswamy, V., Schwarzkopf, M. D., Stouffer, R. J., and Tett, S.: A search for human influences on the thermal structure of the atmosphere, Nature, 382, 39–46, https://doi.org/10.1038/382039a0, 1996.

Satheesh, S. K., Vinoj, V., and Krishna Moorthy, K.: Radiative effects of aerosols at an urban location in southern India: Observations versus model, Atmos. Environ., 44, 5295–5304, https://doi.org/10.1016/j.atmosenv.2010.07.020, 2010.

Schuster, G. L., Dubovik, O., and Holben, B. N.: Angstrom exponent and bimodal aerosol size distributions, J. Geophys. Res.-Atmos., 111, D07207, https://doi.org/10.1029/2005JD006328, 2006.

Sedlacek, A. J., III, Lewis, E. R., Onasch, T. B., Zuidema, P., Redemann, J., Jaffe, D., and Kleinman, L. I.: Using the Black Carbon Particle Mixing State to Characterize the Lifecycle of Biomass Burning Aerosols, Environ. Sci. Technol., 56, 14315–14325, https://doi.org/10.1021/acs.est.2c03851, 2022.

Shinozuka, Y., Saide, P. E., Ferrada, G. A., Burton, S. P., Ferrare, R., Doherty, S. J., Gordon, H., Longo, K., Mallet, M., Feng, Y., Wang, Q., Cheng, Y., Dobracki, A., Freitag, S., Howell, S. G., LeBlanc, S., Flynn, C., Segal-Rosenhaimer, M., Pistone, K., Podolske, J. R., Stith, E. J., Bennett, J. R., Carmichael, G. R., da Silva, A., Govindaraju, R., Leung, R., Zhang, Y., Pfister, L., Ryoo, J.-M., Redemann, J., Wood, R., and Zuidema, P.: Modeling the smoky troposphere of the southeast Atlantic: a comparison to ORACLES airborne observations from September of 2016, Atmos. Chem. Phys., 20, 11491–11526, https://doi.org/10.5194/acp-20-11491-2020, 2020a.

Shinozuka, Y., Kacenelenbogen, M. S., Burton, S. P., Howell, S. G., Zuidema, P., Ferrare, R. A., LeBlanc, S. E., Pistone, K., Broccardo, S., Redemann, J., Schmidt, K. S., Cochrane, S. P., Fenn, M., Freitag, S., Dobracki, A., Segal-Rosenheimer, M., and Flynn, C. J.: Daytime aerosol optical depth above low-level clouds is similar to that in adjacent clear skies at the same heights: airborne observation above the southeast Atlantic, Atmos. Chem. Phys., 20, 11275–11285, https://doi.org/10.5194/acp-20-11275-2020, 2020b.

Sinyuk, A., Holben, B. N., Eck, T. F., Giles, D. M., Slutsker, I., Korkin, S., Schafer, J. S., Smirnov, A., Sorokin, M., and Lyapustin, A.: The AERONET Version 3 aerosol retrieval algorithm, associated uncertainties and comparisons to Version 2, Atmos. Meas. Tech., 13, 3375–3411, https://doi.org/10.5194/amt-13-3375-2020, 2020.

Smirnov, A., Holben, B. N., Kaufman, Y. J., Dubovik, O., Eck, T. F., Slutsker, I., Pietras, C., and Halthore, R. N.: Optical Properties of Atmospheric Aerosol in Maritime Environments, J. Atmos. Sci., 59, 501–523, https://doi.org/10.1175/1520-0469(2002)059<0501:OPOAAI>2.0.CO;2, 2002.

Stein, A. F., Draxler, R. R., Rolph, G. D., Stunder, B. J. B., Cohen, M. D., and Ngan, F.: NOAA's HYSPLIT Atmospheric Transport and Dispersion Modeling System, B. Am. Meteorol. Soc., 96, 2059–2077, https://doi.org/10.1175/BAMS-D-14-00110.1, 2015.

Stier, P., Schutgens, N. A. J., Bellouin, N., Bian, H., Boucher, O., Chin, M., Ghan, S., Huneeus, N., Kinne, S., Lin, G., Ma, X., Myhre, G., Penner, J. E., Randles, C. A., Samset, B., Schulz, M., Takemura, T., Yu, F., Yu, H., and Zhou, C.: Host model uncertainties in aerosol radiative forcing estimates: results from the AeroCom Prescribed intercomparison study, Atmos. Chem. Phys., 13, 3245–3270, https://doi.org/10.5194/acp-13-3245-2013, 2013.

Takemura, T., Nakajima, T., Dubovik, O., Holben, B. N., and Kinne, S.: Single-Scattering Albedo and Radiative Forcing of Various Aerosol Species with a Global Three-Dimensional Model, J. Climate, 15, 333–352, https://doi.org/10.1175/1520-0442(2002)015<0333:SSAARF>2.0.CO;2, 2002.

Tatro, T. and Zuidema, P.: More biomass burning aerosol is being advected westward over the southern tropical Atlantic since 2003, Science Total Environ., 965, 178506, https://doi.org/10.1016/j.scitotenv.2025.178506, 2025.

Taylor, J. W., Wu, H., Szpek, K., Bower, K., Crawford, I., Flynn, M. J., Williams, P. I., Dorsey, J., Langridge, J. M., Cotterell, M. I., Fox, C., Davies, N. W., Haywood, J. M., and Coe, H.: Absorption closure in highly aged biomass burning smoke, Atmos. Chem. Phys., 20, 11201–11221, https://doi.org/10.5194/acp-20-11201-2020, 2020.

Thompson, G. and Eidhammer, T.: A Study of Aerosol Impacts on Clouds and Precipitation Development in a Large Winter Cyclone, J. Atmos. Sci., 71, 3636–3658, https://doi.org/10.1175/jas-d-13-0305.1, 2014.

Twomey, S.: Pollution and the planetary albedo, Atmos. Environ. (1967), 8, 1251–1256, https://doi.org/10.1016/0004-6981(74)90004-3, 1974.

Twomey, S.: The Influence of Pollution on the Shortwave Albedo of Clouds, J. Atmos. Sci., 34, 1149–1152, https://doi.org/10.1175/1520-0469(1977)034<1149:Tiopot>2.0.Co;2, 1977.

Vakkari, V., Beukes, J. P., Dal Maso, M., Aurela, M., Josipovic, M., and van Zyl, P. G.: Major secondary aerosol formation in southern African open biomass burning plumes, Nat. Geosci., 11, 580–583, https://doi.org/10.1038/s41561-018-0170-0, 2018.

van der Werf, G. R., Randerson, J. T., Giglio, L., Collatz, G. J., Mu, M., Kasibhatla, P. S., Morton, D. C., DeFries, R. S., Jin, Y., and van Leeuwen, T. T.: Global fire emissions and the contribution of deforestation, savanna, forest, agricultural, and peat fires (1997–2009), Atmos. Chem. Phys., 10, 11707–11735, https://doi.org/10.5194/acp-10-11707-2010, 2010.

Vermote, E., Ellicott, E., Dubovik, O., Lapyonok, T., Chin, M., Giglio, L., and Roberts, G. J.: An approach to estimate global biomass burning emissions of organic and black carbon from MODIS fire radiative power, J. Geophys. Res.-Atmos., 114, D18205, https://doi.org/10.1029/2008JD011188, 2009.

Wang, Y., Vogel, J. M., Lin, Y., Pan, B., Hu, J., Liu, Y., Dong, X., Jiang, J. H., Yung, Y. L., and Zhang, R.: Aerosol microphysical and radiative effects on continental cloud ensembles, Adv. Atmos. Sci., 35, 234–247, https://doi.org/10.1007/s00376-017-7091-5, 2018.

Waquet, F., Peers, F., Ducos, F., Goloub, P., Platnick, S., Riedi, J., Tanré, D., and Thieuleux, F.: Global analysis of aerosol properties above clouds, Geophys. Res. Lett., 40, 5809–5814, https://doi.org/10.1002/2013GL057482, 2013.

Wilcox, E. M.: Stratocumulus cloud thickening beneath layers of absorbing smoke aerosol, Atmos. Chem. Phys., 10, 11769–11777, https://doi.org/10.5194/acp-10-11769-2010, 2010.

Wilcox, E. M.: Direct and semi-direct radiative forcing of smoke aerosols over clouds, Atmos. Chem. Phys., 12, 139–149, https://doi.org/10.5194/acp-12-139-2012, 2012.

Wu, H., Taylor, J. W., Szpek, K., Langridge, J. M., Williams, P. I., Flynn, M., Allan, J. D., Abel, S. J., Pitt, J., Cotterell, M. I., Fox, C., Davies, N. W., Haywood, J., and Coe, H.: Vertical variability of the properties of highly aged biomass burning aerosol transported over the southeast Atlantic during CLARIFY-2017, Atmos. Chem. Phys., 20, 12697–12719, https://doi.org/10.5194/acp-20-12697-2020, 2020.

Zhang, J. and Zuidema, P.: The diurnal cycle of the smoky marine boundary layer observed during August in the remote

southeast Atlantic, Atmos. Chem. Phys., 19, 14493–14516, https://doi.org/10.5194/acp-19-14493-2019, 2019.

Zhang, J. and Zuidema, P.: Sunlight-absorbing aerosol amplifies the seasonal cycle in low-cloud fraction over the southeast Atlantic, Atmos. Chem. Phys., 21, 11179–11199, https://doi.org/10.5194/acp-21-11179-2021, 2021.

Zhang, Y., Zhang, X., Wang, K., He, J., Leung, L. R., Fan, J., and Nenes, A.: Incorporating an advanced aerosol activation parameterization into WRF-CAM5: Model evaluation and parameterization intercomparison, J. Geophys. Res.-Atmos., 120, 6952–6979, https://doi.org/10.1002/2014JD023051, 2015a.

Zhang, Y., Chen, Y., Fan, J., and Leung, L.-Y. R.: Application of an Online-Coupled Regional Climate Model, WRF-CAM5, over East Asia for Examination of Ice Nucleation Schemes: Part II. Sensitivity to Heterogeneous Ice Nucleation Parameterizations and Dust Emissions, Climate, 3, 753–774, https://doi.org/10.3390/cli3030753, 2015b.

Zhou, S., Collier, S., Jaffe, D. A., Briggs, N. L., Hee, J., Sedlacek III, A. J., Kleinman, L., Onasch, T. B., and Zhang, Q.: Regional influence of wildfires on aerosol chemistry in the western US and insights into atmospheric aging of biomass burning organic aerosol, Atmos. Chem. Phys., 17, 2477–2493, https://doi.org/10.5194/acp-17-2477-2017, 2017.

Zuidema, P., Redemann, J., Haywood, J., Wood, R., Piketh, S., Hipondoka, M., and Formenti, P.: Smoke and Clouds above the Southeast Atlantic: Upcoming Field Campaigns Probe Absorbing Aerosol's Impact on Climate, B. Am. Meteorol. Soc., 97, 1131–1135, https://doi.org/10.1175/bams-d-15-00082.1, 2016.

Zuidema, P., Sedlacek III, A. J., Flynn, C., Springston, S., Delgadillo, R., Zhang, J., Aiken, A. C., Koontz, A., and Muradyan, P.: The Ascension Island Boundary Layer in the Remote Southeast Atlantic is Often Smoky, Geophys. Res. Lett., 45, 4456–4465, https://doi.org/10.1002/2017GL076926, 2018.